LBNL-41872
Preprint

ERNEST ORLANDO LAWRENCE BERKELEY NATIONAL LABORATORY

The Phase Space of the Focusing Cubic Schrödinger Equation: A Numerical Study

Yuri O. Burlakov

Computing Sciences Directorate
Mathematics Department

May 1998

Ph.D. Thesis

REFERENCE COPY
Does Not
Circulate
Bldg. 50 Library - Ref.
Lawrence Berkeley National Laboratory
Copy 1
LBNL-41872

DISCLAIMER

This document was prepared as an account of work sponsored by the United States Government. While this document is believed to contain correct information, neither the United States Government nor any agency thereof, nor the Regents of the University of California, nor any of their employees, makes any warranty, express or implied, or assumes any legal responsibility for the accuracy, completeness, or usefulness of any information, apparatus, product, or process disclosed, or represents that its use would not infringe privately owned rights. Reference herein to any specific commercial product, process, or service by its trade name, trademark, manufacturer, or otherwise, does not necessarily constitute or imply its endorsement, recommendation, or favoring by the United States Government or any agency thereof, or the Regents of the University of California. The views and opinions of authors expressed herein do not necessarily state or reflect those of the United States Government or any agency thereof or the Regents of the University of California.

LBNL-41872

THE PHASE SPACE OF THE FOCUSING CUBIC SCHRÖDINGER EQUATION: A NUMERICAL STUDY*

Yuri O. Burlakov
Lawrence Berkeley National Laboratory
and
Department of Mathematics
University of California
Berkeley, CA 94720, USA

May 1998

Ph.D. Thesis

*This work was supported in part by the Office of Energy Research, Office of Computational and Technology Research, Mathematical, Information, and Computational Sciences Division, Applied Mathematical Sciences Subprogram, of the U.S. Department of Energy, under Contract No. DE-AC03-76SF00098, and by the National Science Foundation under Grants DMS94-14631 and DMS89-19074.

The Phase Space of the Focusing Cubic Schrödinger Equation: A Numerical Study. [1]

by

Yuri O. Burlakov

Diploma (Moscow State University) 1991

A dissertation submitted in partial satisfaction of the
requirements for the degree of
Doctor of Philosophy

in

Mathematics

in the

GRADUATE DIVISION
of the
UNIVERSITY of CALIFORNIA at BERKELEY

Committee in charge:

Professor Alexandre J. Chorin, Chair
Professor Ole H. Hald
Professor Phillip Colella

1998

[1]This work was supported in part by the Applied Mathematical Sciences Subprogram of the Office of Energy Research, U.S. Department of Energy, under contract DE-AC03-76-SF00098, and in part by the National Science Foundation under grants DMS94-14631 and DMS89-19074.

The Phase Space of the Focusing Cubic Schrödinger Equation: A Numerical Study

Copyright © 1998

by

Yuri O. Burlakov

The U.S. Department of Energy has the right to use this document
for any purpose whatsoever including the right to reproduce
all or any part thereof

Contents

List of Figures v

List of Tables vii

1 Introduction 1

2 Some Basic Facts from Statistical Mechanics 5
- 2.1 Some Basic Concepts and Definitions 5
- 2.2 The Microcanonical Ensemble 6
- 2.3 The Canonical Ensemble 8
- 2.4 Energy Fluctuations in the Canonical Ensemble 9
- 2.5 Finite Size Effects and Phase Transitions 11

3 The Non-linear Schrödinger Equation and Measure 15
- 3.1 The Canonical Ensemble Associated with the Cubic Schrödinger Equation . 15
- 3.2 Ergodicity 17
- 3.3 Numerical Methods 19
  - 3.3.1 Metropolis Sampling Method 19
  - 3.3.2 Details of the Implementation of the Metropolis Sampling 24
  - 3.3.3 Numerical Method for Integration of the Schrödinger equation . . . 25
- 3.4 Comparison of the Time and Ensemble Averages 26

4 Phase Space Topological Changes and Bifurcation 29
- 4.1 The History of the Problem 29
- 4.2 Definitions 36
- 4.3 Simple case 37
  - 4.3.1 Phase space splitting of the dynamical system into energy level sets 38
  - 4.3.2 Changes of Metropolis sampling trajectories with respect to temperature 42
  - 4.3.3 Changes of Metropolis sampling trajectories with respect to constraint N 46
- 4.4 General case 50

4.4.1 Changes of Metropolis sampling trajectories with respect to temperature in large system. 52
4.4.2 Changes of Metropolis sampling trajectories with respect to constraint N in large system 55
4.4.3 Changes in kurtosis K as constraint N increases 56
4.4.4 Changes in kurtosis K as the number of discretization points increases 58
4.4.5 Changes in kurtosis K as both N and the number of discretization points increase 59

5 The Self-Induction Approximation and the Non-linear Schrödinger Equation 62
5.1 Introduction. Turbulence and Statistical Mechanics. 62
5.2 The Self-Induction Approximation 64
5.3 The Hasimoto Transformation 69
5.4 Changes in the shape of a vortex filament with respect to constraint N and temperature 74

6 Conclusions 77

Bibliography 80

List of Figures

2.1 Phase transition in magnets. Below the critical temperature T_c magnetization is nonzero, above the critical temperature T_c magnetization is zero. 13

2.2 The smooth curves represent the functions of temperature for the finite N. The discontinuous step function represents the limit of the smooth functions as $N \to \infty$. 14

3.1 Equivalence of the ensemble (3.5), (3.6) and the microcanonical ensemble. . 27

3.2 Time average and ensemble average 28

4.1 Typical real and imaginary components of the field for low temperature and large constraint. 30

4.2 Typical real and imaginary components of the field for high temperature. . 31

4.3 Typical real and imaginary components of the field for low temperature and small constraint. 31

4.4 Plot of $S(x)/S^0(x)$ for high and low temperatures 33

4.5 Values of K for fixed N=80, and varying β. 34

4.6 Values of K for N= 10, 40, 80 and varying β. 35

4.7 Time trajectories in the phase space of the 4-dimensional system with constraint. The axes correspond to the two real components and one of the imaginary components of the system. The thick line corresponds to the minimum value of the Hamiltonian. The thin line corresponds to a value of the Hamiltonian larger than the minimum. 39

4.8 Trajectories in the phase space of the 4-dimensional system with constraint. The axes correspond to the two real components and one of the imaginary components of the system. The thick line in this picture is the same minimum energy line as in the figure (4.7) above, and is reproduced in this picture as a reference line. 40

4.9 Trajectories in the phase space of the 4-dimensional system with constraint. The axes correspond to the two real components and one of the imaginary components of the system. Thick line corresponds to the minimum of the Hamiltonian, and thin line corresponds to the maximum of the Hamiltonian. 41

4.10 Metropolis sampling trajectory of the 4-dimensional system, β=4. The axes correspond to the two real components and one of the imaginary components of the system. 42
4.11 Metropolis sampling trajectories of the 4-dimensional system with constraint, β=0.04. The axes correspond to the two real components and one of the imaginary components of the system. 43
4.12 Density of states for the Metropolis sampling trajectories. The horizontal axis is the energy, from smallest to largest possible values. The vertical axis is the density of the configuration with each energy. 44
4.13 Density of states for the Metropolis sampling trajectories. The horizontal axis is the energy, from smallest to largest possible values. The vertical axis is the density of the configuration with each energy. 45
4.14 Values of K for N= 1, 10, 40 and varying β. 46
4.15 Metropolis sampling trajectories of the 2 node system, $N = 1$, $1/(\beta N) = 10^{-2}$. 47
4.16 Metropolis sampling trajectories of the 2 node system, $N = 10$, $1/(\beta N) = 10^{-2}$. 48
4.17 Metropolis sampling trajectories of the 2 node system, $N = 40$, $1/(\beta N) = 10^{-2}$. 48
4.18 Metropolis sampling trajectories of the 2 node system, $N = 40$, $1/(\beta N) = 1$. 49
4.19 Metropolis sampling trajectories of the 2 node system, $N = 40$, $1/(\beta N) = 10$. 50
4.20 Splitting of the minimum energy circle in the time dependent system, $N = 10$. 51
4.21 Splitting of the minimum energy circle in the time dependent system, $N = 40$. 51
4.22 Metropolis sampling trajectory for the 10-point system, N=1, $\beta = 4$. 53
4.23 Metropolis sampling trajectory for the 10-point system, N=1, $\beta = 0.1$. . . . 54
4.24 Projected time trajectory of the 10-point system for small energy. 54
4.25 Metropolis sampling trajectory for the 40-point system $N = 10^3$, $\beta = 10^{-4}$. 55
4.26 Metropolis sampling trajectory for the 40-point system $N = 10^3$, $\beta = 10^{-5}$. 56
4.27 Metropolis sampling trajectory for the 40-point system $N = 10^3$, $\beta = 10^{-6}$ 57
4.28 Values of K for various N and β 57
4.29 Values of K for N=40 and different number of discretization points. 58
4.30 Values of K for N=80 and different number of discretization points. 59
4.31 Values of K for increasing number of discretization points and N. $N = 640$ (for 40 and 80 nodes), $N = 1000$ (for 160 nodes), and $N = 2000$ (for 320 nodes) 61

5.1 Typical vortex filament for low temperature and large N, $\frac{1}{\beta N} = 10^{-2}$ 75
5.2 Typical vortex filament for low temperature and small N, $\frac{1}{\beta N} = 10^{-2}$ . . . 76
5.3 Typical vortex filament for high temperature, $\frac{1}{\beta N} = 10$ 76

List of Tables

4.1 Maximum absolute value of the derivative 60

Acknowledgements

I wish to thank my advisor, Alexandre Chorin, without whose mathematical guidance this thesis would have been impossible. I would like to thank Alexandre for his support and encouragement during all of my time in the graduate school, and especially during the difficult period in my life.

I am very grateful to the members of the Mathematics group at LBNL for many helpful conversations. Especially I would like to thank David Adalsteinsson for his help.

I wish to thank Donald Krapp for careful reading of this thesis.

Finally I wish to thank all of my friends for their support during the work on this thesis.

Chapter 1

Introduction

The nonlinear Schrödinger equation plays a major role in describing various physical phenomena in continuum mechanics, plasma physics, nonlinear optics, and vortex dynamics in classical and superfluid mechanics [23]. In a paper of 1988 [41] on statistical mechanics of the nonlinear Schrödinger equation, it was observed that a Gibbs canonical ensemble associated with the nonlinear Schrödinger equation exhibits behavior reminiscent of a phase transition in classical statistical mechanics. The existence of a phase transition in the canonical ensemble of the nonlinear Schrödinger equation would be very interesting and would have important implications for the role of this equation in modeling physical phenomena; it would also have an important bearing on the theory of weak solutions of nonlinear wave equations [46], [47], [48].

The cubic Schrödinger equation, as will be shown later, is equivalent to the self-induction approximation for vortices, which is a widely used equation of motion for a thin vortex filament in classical and superfluid mechanics [26]. The existence of a phase transi-

tion in such a system would be very interesting and actually very surprising for the following reasons: in classical fluid mechanics it is believed that the turbulent regime is dominated by strong vortex stretching [14], while the vortex system described by the cubic Schrödinger equation does not allow for stretching. In superfluid mechanics the self-induction approximation and its modifications have been used to describe the motion of thin superfluid vortices [53], which exhibit a phase transition; however, more recently some authors concluded that these equations do not adequately describe superfluid turbulence [5], and the absence of a phase transition in the cubic Schrödinger equation would strengthen their argument. The self-induction approximation for vortices takes into account only very localized interactions, and the existence of a phase transition in such a simplified system would be very unexpected.

In this thesis we present a numerical study of the phase transition type phenomena observed in [41]; in particular, we find that these phenomena are strongly related to the splitting of the phase space into distinctly different components. We point out the interesting fact that the phase transition type behavior of the discretized cubic Schrödinger equation can be observed in a discretization with as few as 2 points. The refinement of the discretization does not change the global picture qualitatively.

We vary two parameters in the canonical ensemble of the cubic Schrödinger equation: the first parameter is the temperature, the second one is a certain constraint on the function space. We demonstrate that at a fixed low temperature, as the constraint varies, the canonical ensemble of the cubic Schrödinger equation undergoes a bifurcation which is manifested both in the change in the shape of the typical function and in a corresponding

change of the structure of the phase space.

For a fixed value of the constraint, as temperature varies there is a phase transition type change in shape of the typical function and a corresponding change in the structure of the phase space. We investigate numerically a special continuum limit in which both the constraint and the number of discretization points increase, and conclude that there is a strong indication of a phase transition in this limit. We also discover that in terms of vortex approximations, the phase transition type behavior for the cubic Schrödinger equation results in the transition from an almost straight filament with a sharp kink for low temperatures to a filament of random shape at high temperatures. We remark that in the limit the temperature at which the transition occurs increases to infinity, which is in agreement with the results of Chorin [12], [14], [15] that the single vortex filament has a phase transition at infinite temperature.

Recently there has been an increasing interest in the study of motion of a single thin vortex and of a collection of thin vortices in the approximations of the self-induction type [31], [32], [33], [34], [30], [57]. If the phase transition in the cubic Schrödinger equation were to exist, this might lead to a reconsideration of the role of these equations and their modifications in the study of classical and superfluid turbulence.

This thesis consists of six chapters. Chapter 1 is an introduction and a brief summary of our results.

In Chapter 2 we present some essential facts from classical statistical mechanics that we will need in subsequent chapters.

In Chapter 3, following [41] we introduce the statistical ensemble for the non-linear

Schrödinger equation, which is similar to the classical Gibbs canonical ensemble. We discuss the properties of this ensemble, in particular its invariance [46]. We show that this ensemble is, in a sense to be made precise later, equivalent to the microcanonical ensemble. Then we discuss the ergodicity of the non-linear Schrödinger equation. We present numerical results that show the equivalence of the time and ensemble averages.

In Chapter 4 we begin by considering a simplified system that arises from the discretization of the non-linear Schrödinger equation. We study the energy level sets of the dynamical system, and the configurations in the phase space on which the statistical ensemble of the cubic Schrödinger equation is concentrated. We observe that as we vary temperature and a constraint in the Gibbs ensemble, there are two distinctly different structures in the phase space - one has a ball-like shape, and the other has a torus-like shape. These different shapes appear at the same temperature as the phase transition type behavior observed in [41]. These ball and torus structures exist for any discretization of the system, starting from the simplest 2-point discretization. We show that in a certain limit there is a strong evidence of a discontinuity in a temperature dependent quantity.

In Chapter 5 we derive a self-induction approximation of the motion of a single vortex filament, following the presentations in [3] and [6]. We briefly mention the properties of the self-induction approximation like the conservation of the arclength of the filament. Using the Hasimoto transformation [26] we derive the cubic Schrödinger equation. We discuss briefly a few constants of motion of the the cubic Schrödinger equation and the corresponding constants of motion of the self-induction approximation.

Chapter 6 contains final remarks and conclusions.

Chapter 2

Some Basic Facts from Statistical Mechanics

In this chapter we present basic concepts from statistical mechanics; more detailed exposition can be found in [28],[39].

2.1 Some Basic Concepts and Definitions

Suppose we are interested in the properties of a large system of interacting particles at equilibrium. By equilibrium we mean the state of the system where thermodynamic properties (pressure, volume, and temperature, for example) do not change in time; we are not concerned with how the system reaches an equilibrium. One example of such a system is an ideal gas consisting of N particles. A state of this system is completely determined by the 3N canonical coordinates q_{i1}, q_{i2}, q_{i3} and 3N canonical momenta p_{i1}, p_{i2}, p_{i3}. Suppose that the dynamics of this system are described by the Hamiltonian H(p,q), where we use

the notation $p = (p_{11}, p_{12}, p_{13}, \ldots, p_{N1}, p_{N2}, p_{N3})$, $q = (q_{11}, q_{12}, q_{13}, \ldots, q_{N1}, q_{N2}, q_{N3})$; the Hamiltonian H(p,q) is a map from $\mathbf{R}^{6N}$ into $\mathbf{R}$; then the equations of motions are:

$$\dot{q}_i = \frac{\partial H(p,q)}{\partial p_i}$$
$$\dot{p}_i = -\frac{\partial H(p,q)}{\partial q_i}. \tag{2.1}$$

Each configuration of the system corresponds to a point in the 6N dimensional space. If we specify some initial condition with an energy E, then our system will move in space on the surface of constant energy E. We are not interested in the motion of the one particular configuration of the system, in fact we cannot identify it in practice due to the large number of particles in our system. Instead, we would like to consider many possible microscopic states of the system (points in our 6N dimensional space) that correspond to a single macroscopic state; we also would like to find out what would be an appropriate distribution of the states at equilibrium for the system under consideration.

2.2 The Microcanonical Ensemble

We begin our discussion with a description of the microcanonical ensemble. Define an energy shell as all points (p,q) in the 6N dimensional space with the values of energy H(p,q) at these points between E and $E + \delta E$, where $\delta E \ll E$. We make the following assumption: When a macroscopic system is in thermodynamic equilibrium, every state in the same energy shell is equally likely. Therefore at the thermodynamic equilibrium the

probability density function to find a system in a state (p,q) is given by:

$$\rho(p,q) = \begin{cases} Constant & \text{if } E < H(p,q) < E + \delta E \\ 0 & \text{otherwise} \end{cases}$$

If f(p,q) is a measurable function then its ensemble average is defined as

$$< f >= \frac{\int f(p,q)\rho(p,q)dpdq}{\int \rho(p,q)dpdq}. \tag{2.2}$$

Every system in the microcanonical ensemble consists of N particles, has a volume V, and an energy between E and $E + \delta E$. Now we define two fundamental concepts of statistical mechanics - entropy and temperature. Let D(E) be the volume occupied by a microcanonical ensemble in the phase space:

$$D(E) = \int_{E<H(p,q)<E+\delta E} \rho(p,q)dpdq. \tag{2.3}$$

Entropy is defined to be:

$$S(E,V) = k \log D(E), \tag{2.4}$$

where k is the Boltzmann constant, which is not important for our presentation, so we will choose units in which it is equal to 1. The entropy is an extensive variable: that is, when the system is composed of two subsystems, the total entropy is equal to the sum of the entropies of the subsystems:

$$S(E,V) = S(E_1,V_1) + S(E_2,V_2). \tag{2.5}$$

Let us consider a system which is composed of two subsystems. The total energy of such a system, neglecting the interaction energy between these subsystems, is:

$$E = E_1 + E_2. \tag{2.6}$$

The volume of the phase space that these two subsystems occupy is proportional to:

$$D(E_1)D(E_2). \tag{2.7}$$

Consider a system at equilibrium with an energy E which is composed of two subsystems with energy E_1 and E_2 respectively. The entropy of the system is equal to $S(E,V) = S(E_1,V_1) + S(E_2,V_2)$. Consider the problem of maximizing the entropy of the system $S(E,V)$ subject to the constraint $E = E_1 + E_2$, i.e.:

$$\begin{aligned} &maximize \quad S(E,V) \\ &subject\ to \quad E = E_1 + E_2 \end{aligned} \tag{2.8}$$

By using Lagrange multipliers we can solve the constrained maximization problem (2.9) to get the following necessary condition for the maximum:

$$\left.\frac{\partial S_1(E_1)}{\partial E_1}\right|_{E_1=\bar{E}_1} = \left.\frac{\partial S_2(E_2)}{\partial E_2}\right|_{E_2=\bar{E}_2}, \tag{2.9}$$

The minimum of entropy is achieved at some energy values $\bar{E}_1$ and $\bar{E}_2$. Using condition (2.9) define temperature T:

$$\frac{1}{T} \equiv \left.\frac{\partial S_1(E_1)}{\partial E_1}\right|_{E_1=\bar{E}_1} = \left.\frac{\partial S_2(E_2)}{\partial E_2}\right|_{E_2=\bar{E}_2}. \tag{2.10}$$

From this definition temperature is a parameter which arises through an equilibrium condition.

2.3 The Canonical Ensemble

Now we would like to find out what is a relevant ensemble for description of a system in thermal equilibrium with a larger system. In other words, we have to find out

the probability that system 1 in thermal contact with a larger system 2 has energy E_1. As above, consider two systems in thermal equilibrium. We showed that the total entropy is maximal for some particular values of energy $\bar{E}_1$ and $\bar{E}_2$. Assume that the number of particles in system 1, which we denote by N1 is much smaller than the number of particles in system 2, which we denote by N2, i.e. $N_1 \ll N_2$; and also assume that $\bar{E}_1 \ll \bar{E}_2$. The event of finding the system 1 in the $dp_1 dq_1$ of (p_1, q_1) is independent of the event of finding system 2 in the state with energy E_2. Therefore the probability of finding the system 1 in the $dp_1 dq_1$ neighborhood of (p_1, q_1) is proportional to $dp_1 dq_1 D_2(E_2)$; from this it follows that $\rho(p_1, q_1)$ is proportional to $D_2(E_2)$. By assumption E_1 is much smaller than E; expand $\log D_2(E - E_1)$ in a Taylor series and keep the first two terms in the expansion:

$$\log D_2(E - E_1) \equiv S_2(E - E_1) \approx S_2(E) - E_1 \frac{\partial S_2(E_2)}{\partial E_2}\bigg|_{E_2=E} = S_2(E) - E_1 \frac{1}{T}. \tag{2.11}$$

Taking the logarithm of both sides yields:

$$D_2(E - E_1) \approx \exp(S_2(E)) \exp(-\frac{E_1}{T}). \tag{2.12}$$

The first term in (2.12) does not depend on E_1, so it is just a proportionality constant. This implies that the probability $\rho(p_1, q_1)$ of system 1 to have energy E_1 in equilibrium with the larger system is proportional to:

$$\exp(-\frac{E_1}{T}). \tag{2.13}$$

2.4 Energy Fluctuations in the Canonical Ensemble

We are going to show that the microcanonical ensemble is equivalent in a certain sense to the canonical ensemble. We compute the mean square fluctuation of the energy in

the canonical ensemble; and show that the fluctuation decreases as the number of particles in the system increases. This suggests that the canonical distribution is sharply peaked around its mean. The expected value of the energy in the canonical ensemble is:

$$< H >= \frac{\int H e^{-\beta H} dpdq}{\int e^{-\beta H} dpdq}. \tag{2.14}$$

Introduce the partition function:

$$Z(V,T) = \int e^{-\beta H} dpdq. \tag{2.15}$$

Define the quantity A(V,T)

$$-\beta A(V,T) = \log Z(V,T), \tag{2.16}$$

which is actually called the Helmholtz free energy. Differentiate the following identity with respect to β;

$$\int e^{\beta(A(V,T)-H(p,q))} dpdq = 1, \tag{2.17}$$

to obtain:

$$\int e^{\beta(A(V,T)-H(p,q))}[A(V,T) - H(p,q) + \beta\frac{\partial A}{\partial \beta}]dpdq = 0. \tag{2.18}$$

Integrating the expression (2.18) above we have:

$$A(V,T) - < H > + \beta\frac{\partial A}{\partial \beta} = 0. \tag{2.19}$$

Equation (2.14) can be rewritten as:

$$< H > - \int H e^{\beta(A(V,T)-H)} dpdq = 0. \tag{2.20}$$

Differentiate this equation with respect to β to obtain:

$$\frac{\partial < H >}{\partial \beta} - \int H(A(V,T) - H + \beta \frac{\partial A}{\partial \beta}) e^{\beta(A(V,T)-H)} dpdq = 0, \tag{2.21}$$

which implies:

$$\frac{\partial < H >}{\partial \beta} + \int (< H > - H(p,q))(A(V,T) - H(p,q) + \beta \frac{\partial A}{\partial \beta}) e^{\beta(A(V,T)-H(p,q))} dpdq = 0. \tag{2.22}$$

Taking into account equation (2.19) we can rewrite (2.22) in the form:

$$\frac{\partial < H >}{\partial \beta} + \int (< H > - H(p,q))^2 e^{\beta(A(V,T)-H(p,q))} dpdq = 0. \tag{2.23}$$

Using equation (2.16) we obtain:

$$\frac{\partial < H >}{\partial \beta} + < (< H > - H)^2 > = 0. \tag{2.24}$$

We can also rewrite this equation as:

$$T^2 \frac{\partial < H >}{\partial T} + < (< H > - H)^2 > = 0. \tag{2.25}$$

For a macroscopic system $< H > \propto N$ and $\frac{\partial < H >}{\partial T} \propto N$, thus as $N \to \infty$ the mean square fluctuation goes to zero; in this sense the canonical ensemble is equivalent to the micro-canonical ensemble.

2.5 Finite Size Effects and Phase Transitions

We formulated the statistical ensemble for a system of fixed size: i.e., a fixed number of particles N, and a fixed volume V. However, we are interested in the properties of a system consisting of a huge number of particles (on the order of 10^{23}). Therefore we

take a limit in which the number of particles N and the volume V both go to infinity, but the ratio V/N remains fixed. This limit is called a thermodynamic limit:

$$< X >_{\infty} = \lim_{N \to \infty, V \to \infty} < X >_{N,V} . \tag{2.26}$$

To simulate 10^{23} degrees of freedom is out of reach of computers, and in practice the number of degrees of freedom used for computation is much smaller, of the order of a few thousand. Nevertheless, even with such a modest number of degrees of freedom some useful results can still be obtained.

Some physical systems in nature exhibit phase transitions (gas-liquid, fluid-superfluid, conductor-superconductor, magnetization transition etc.), i.e. a sharp change of some properties of the system with respect to the change in some parameter, such as temperature. Two important questions are: Can we determine whether a mathematical model exhibits a phase transition? And can we see a phase transition on a computer (that is to say in a simulation with just a finite, probably very small, number of degrees of freedom) ? The answer to the first question is yes, but very often it is difficult to do so. The answer to the second question may depend on a number of subtle assumptions. We do not pursue both of these questions further here, but limit ourselves to a brief discussion of phase transitions and effects associated with the finite size of a system and the canonical ensemble.

For a system of finite size, the expected value of some smooth or analytic function is a smooth or analytic function of the parameter β. However, if we take a thermodynamic limit, as the size of the system goes to infinity, then some quantity of interest might become nonsmooth and nonanalytic with respect to β. Therefore a typical definition of a phase transition is the following. Let X be a smooth or analytic measurable function: If

$\lim_{N\to\infty, V\to\infty} < X > (\beta)$ is a nonanalytic function of β then we say that the system exhibit a phase transition. The temperature $T = \frac{1}{\beta}$ at which this nonanalyticity occurs is called a critical temperature. In this discussion we implicitly assume that temperature is a control parameter of the phase transition.

For the magnetization transition, for example, the typical phase change picture looks like this (see Figure (2.1)).

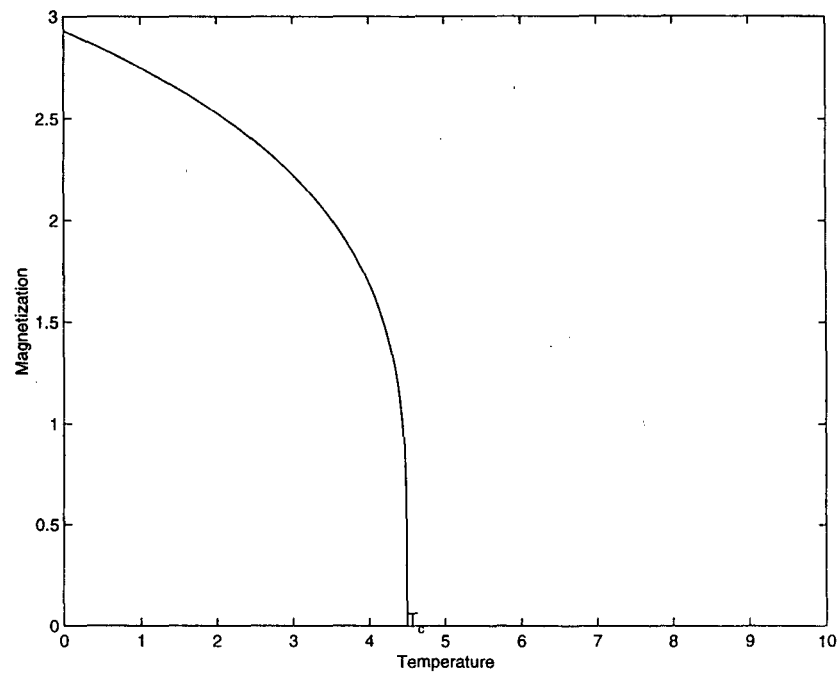

Figure 2.1: Phase transition in magnets. Below the critical temperature T_c magnetization is nonzero, above the critical temperature T_c magnetization is zero.

For values of temperatures below the critical T_c there is a non-zero magnetization; for values of temperature above the critical temperature the magnetization is zero. This type of the phase transition with a discontinuity in the derivative of a function is a called a phase transition of second order. A phase transition with a discontinuity in the function itself is called a phase transition of the first order. A typical picture of a phase transition

of the first order is presented in Figure (2.2).

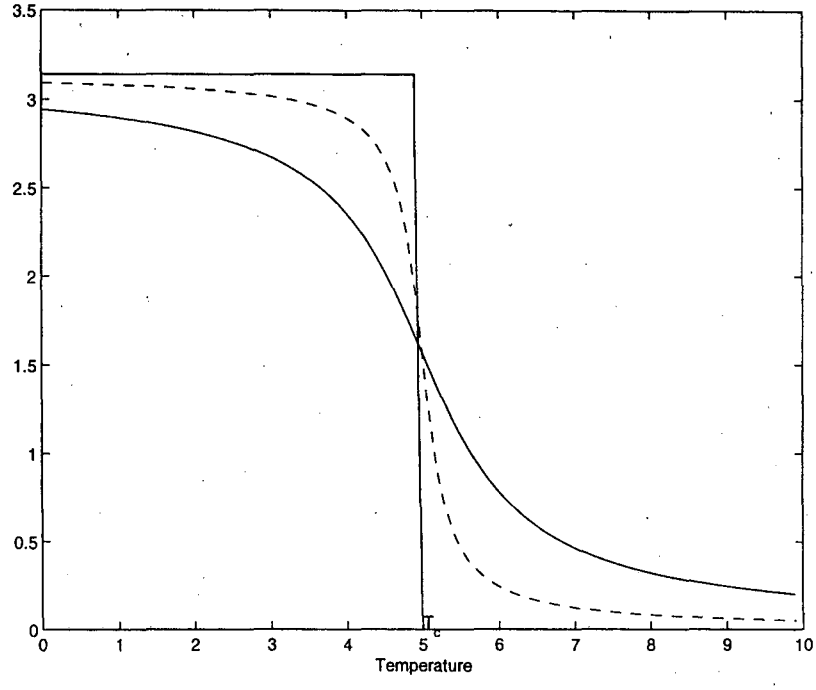

Figure 2.2: The smooth curves represent the functions of temperature for the finite N. The discontinuous step function represents the limit of the smooth functions as $N \to \infty$.

Chapter 3

The Non-linear Schrödinger Equation and Measure

3.1 The Canonical Ensemble Associated with the Cubic Schrödinger Equation

The cubic Schrödinger equation

$$\frac{1}{i}\frac{\partial \psi}{\partial t} = \frac{\partial^2 \psi}{\partial x^2} + \frac{1}{2}|\psi|^2\psi \tag{3.1}$$

which we are going to derive later in Chapter 5 can be rewritten in the Hamiltonian form:

$$\dot{q} = -p'' - p(q^2 + p^2), \qquad \dot{p} = q'' + q(q^2 + p^2), \tag{3.2}$$

where the Hamiltonian is

$$H(p,q) = \frac{1}{2}\int_0^L ((q')^2 + (p')^2)dx - \frac{1}{4}\int_0^L (q^2 + p^2)^2 dx. \tag{3.3}$$

q and p stand respectively for real and imaginary part of the function ψ in (3.1). We use a dot to denote the derivative with respect to time, and a prime to denote the derivative with respect to space; we assume here and everywhere in this thesis that p and q are periodic functions of x.

Lebowitz, Rose, and Speer ([41]) introduced an ensemble very similar to the Gibbs canonical ensemble, with a measure formally written as:

$$\mathbf{P}(dp, dq) = Z^{-1} \exp[-\beta H(p, q)] dp dq, \tag{3.4}$$

or, writing the Hamiltonian explicitly:

$$\mathbf{P}(dp, dq) = Z^{-1} \exp[-\beta \frac{1}{2} \int_0^L ((q')^2 + (p')^2) dx] \exp[\beta \frac{1}{4} \int_0^L (q^2 + p^2)^2 dx] dp dq, \tag{3.5}$$

where dpdq is a Lebesgue measure, Z is a partition function, and β is a scalar, the 'inverse temperature'. The Hamiltonian (3.3) is not bounded below, so in order to make sense out of the formal object (3.4), Lebowitz et al. ([41]) suggested to restrict the ensemble to the functions that satisfy either

$$\int_0^L (q^2 + p^2) dx = N, \tag{3.6}$$

or

$$\int_0^L (q^2 + p^2) dx \leq N, \tag{3.7}$$

for some constant N. The idea is to restrict the set of functions by the constraint (3.6) or (3.7), so that the second term in (3.5) can be bounded by the first term in (3.5). They proved that this constrained measure is well defined (see ([41]) for details). The meaning

of the first integral in (3.5) is easy to explain; the formal expression

$$\exp(-\beta\frac{1}{2}\int_0^L((q')^2+(p')^2)dx) \tag{3.8}$$

stands for the standard Brownian bridge measure in two dimensions. The second term in (3.5), formally given by

$$\exp(\beta\frac{1}{4}\int_0^L(q^2+p^2)^2dx) \tag{3.9}$$

is a density which can be bounded by the first term (3.8) under the constraint conditions (3.6) or (3.7). The choice of these constraints was motivated by the fact that the nonlinear Schrödinger equation conserves the integral (3.6). This measure was also studied by H.P.McKean ([46]), who showed that this measure is invariant. An invariant measure is by definition a measure that is preserved by the flow of the partial differential equation; this can be described as follows: Take some measurable set of initial conditions and evolve it in time by the nonlinear Schrödinger equation; then the set of solutions at any later time will have the same measure as the initial set.

3.2 Ergodicity

Now we are going to make a connection between the ensemble averages defined by (3.5), (3.6), and the averages in time of the dynamical system (3.2). The average in time of some function f is defined as

$$< f >_t = \frac{1}{t}\int_0^t f(p(s),q(s))ds \tag{3.10}$$

where (p(s),q(s)) is a solution of the equations of motion (3.2) with periodic boundary conditions in space, and with an intitial condition (q(0),p(0)). If the average with respect

to the ensemble is equal to the average in time as time goes to infinity, the dynamical system with such a measure is called ergodic. The importance of this concept is due to the following problem. Very often it is necessary to compute the average in time of a dynamical system; however, integration in time of the equations of motion for large time may be too expensive. In this case, computing ensemble averages might be an attractive alternative.

However, proving ergodicity of a system may be an even more complicated problem; in fact, we do not know any proof of ergodicity for our system. Nevertheless, we have numerical evidence which supports the ergodicity assumption.

There is a natural question that arises at this point: The Hamiltonian (3.3) of the dynamical system (3.2) is a constant of the motion. If we start the dynamical system at some initial configuration with some specific value of the energy $\bar{E}$, the system will have the same energy for all time. Therefore the phase space accessible to the dynamical system is restricted by the Hamiltonian. On the other hand, the average with respect to the measure (3.5),(3.6) is taken over all possible configurations in the phase space subject to a constraint (3.6). Why do we expect the ensemble average (3.5),(3.6) which samples configurations over all possible energy values to give the same result as the time average? If we would like to construct a measure, such that a dynamical system with this measure is ergodic, it seems more natural to consider the microcanonical ensemble since it samples the given energy shell; we choose the energy shell that is defined by $\bar{E}$. However, suppose the measure (3.5),(3.6) is concentrated on the configurations of the energy shell defined by $\bar{E}$; then it is plausible that the averages with respect to (3.5),(3.6) and the microcanonical ensemble will be the same. In this sense the measure (3.5),(3.6) and the microcanonical

ensemble are equivalent.

3.3 Numerical Methods

Our goal now is to evaluate numerically the ensemble average (3.5),(3.6). First we are going to introduce a discretization of the Hamiltonian (3.3) and the constraint (3.6). Discretize the interval [0,L] by n discretization points; let u_i and v_i be the discretization of the real and imaginary part of the solution of the cubic Schrödinger equation; then the discrete version of the Hamiltonian (3.3) is

$$H = \frac{1}{2}\sum_{i=1}^{n}((\frac{u_{i+1}-u_i}{h})^2 + (\frac{v_{i+1}-v_i}{h})^2)h - \frac{1}{4}\sum_{i=1}^{n}(u_i^2+v_i^2)^2 h, \tag{3.11}$$

where h = $\frac{L}{n}$ is the discretization step. This particular discretization of the Hamiltonian leads to the following discretization of the measure (3.5)

$$\mathbf{P}(du,dv) = Z_n^{-1}\exp[-\beta[\frac{1}{2}\sum_{i=1}^{n}((\frac{u_{i+1}-u_i}{h})^2 + (\frac{v_{i+1}-v_i}{h})^2)h - \frac{1}{4}\sum_{i=1}^{n}(u_i^2+v_i^2)^2 h]]dudv, \tag{3.12}$$

and the discretization of the constraint (3.6) is

$$N = \sum_{i=1}^{n}(u_i^2+v_i^2)h. \tag{3.13}$$

3.3.1 Metropolis Sampling Method

We are going to describe a method for computing ensemble averages due to Metropolis et al. ([49]). For the purposes of the presentation assume for a moment that we are given the discrete Hamiltonian $H(x)$ without a constraint, where x denotes a configuration $(X_1,\ldots,X_M)$; and each X_i is a scalar. One can think of x as of $(u_1,v_1,\ldots,u_n,v_n)$ in

the discretization of the Hamiltonian (3.11). However at this point we consider a method without a constraint; later we will add a constraint to the method.

The idea of the method is to construct a Markov chain in the space of all discrete configurations that will converge to the stationary (or equilibrium) probability density π given by $Z^{-1}\exp(-\beta H(X_1,\ldots,X_M))$. Z is a partition function and is the sum of the weights $\exp(-\beta H(X_1,\ldots,X_M))$ over all possible configurations.

$$Z = \int_{\mathbf{R}^M} \exp(-\beta H(X_1,\ldots,X_M))dX_1\ldots dX_M. \tag{3.14}$$

One major difficulty in evaluating the ensemble average is that the partition function Z cannot be easily computed; the Metropolis sampling allows one to avoid this difficulty. The weight of the configuration x is given by:

$$\pi_x = Z^{-1}\exp(-\beta H(X_1,\ldots,X_M)). \tag{3.15}$$

where the subscript x denotes the configuration $(X_1,\ldots,X_M)$.

Given an equilibrium distribution π we wish to construct a Markov chain P that converges to this equilibrium distribution. We need to find a transition probability matrix P = (p_{xy}) = (probability to make a transition from a state x to a state y) that satisfies the following two conditions (for more details see (Binder,Heermann [4]) and (Sokal [55])): Denote by $p_{xy}^{(n)}$ a transition probability from x to y in n steps. *Irreducibility*: For each pair of states x,y there exists an $n \geq 0$, such that $p_{xy}^{(n)} > 0$.

Stationarity of π:

$$\sum_x \pi_x p_{xy} = \pi_y, \quad \forall y. \tag{3.16}$$

A sufficient condition for stationarity of π is:

Detailed balance for π: For each pair of states x and y, $\quad \pi_x p_{xy} = \pi_y p_{yx}$.

A method for constructing a transition probability satisfying the detailed balance condition was introduced by Metropolis et al ([49]). The idea is to take an arbitrary irreducible transition matrix $P^0 = (p^0_{xy})$, called the proposal matrix. In the next section we give an example of the proposal matrix that we use to compute the ensemble averages. Using this matrix P^0 generate a move x↦y; then accept or reject this move with probability b_{xy} or $1 - b_{xy}$ respectively. Thus, the transition probability matrix $P = (p_{xy})$ is:

$$p_{xy} = p^0_{xy} b_{xy} \quad for\ x \neq y \tag{3.17}$$

$$p_{xx} = p^0_{xx} + \sum_{x \neq y} p^0_{xy}(1 - b_{xy}).$$

Detailed balance for the matrix P is equivalent to the following condition:

$$\pi_x p^0_{xy} b_{xy} = \pi_y p^0_{yx} b_{yx}. \tag{3.18}$$

One way to construct b_{xy} is to look for b_{xy} of the following form:

$$b_{xy} = F(\frac{\pi_y p^0_{yx}}{\pi_x p^0_{xy}}), \tag{3.19}$$

where F is a scalar function, F:[0,∞)↦[0,1]. It is easy to see that if F satisfies the following equation:

$$F(\alpha) = \alpha F(\frac{1}{\alpha}), \tag{3.20}$$

then the detailed balance equation (3.18) is satisfied.

There are many different functions satisfying equation (3.20). One suitable choice of F is to take:

$$F(\alpha) = \min(\alpha, 1). \tag{3.21}$$

Another choice of F also used is $F(\alpha) = \frac{\alpha}{\alpha+1}$. Observe that we have a lot of freedom in choosing a proposal matrix P^0; many different proposal moves are possible as long as the matrix P of the full algorithm is irreducible, we also have many different choices of F, as long as they satisfy equation (3.20). At this point we can summarize the algorithm as follows:

1. Generate a proposed move x$\mapsto$y.

2. Compute the ratio:

$$R = \frac{\pi_y p^0_{yx}}{\pi_x p^0_{xy}}. \tag{3.22}$$

3. Accept the transition from x to y with probability F(R). In other words, generate a random number γ from the uniform distribution on [0,1], and accept the proposed move if $\gamma \leq F(R)$, and otherwise reject it. When we reject a proposed move we make a null transition, i.e. we count the old configuration as a new configuration.

4. Calculate the necessary averages.

In equation (3.22): the probabilities of configurations π_x and π_y enter the expression as a ratio, and the partition function Z cancels out. This fact is crucial, since Z is almost never explicitly computable.

When the proposal matrix P^0 is symmetric, i.e. $p^0_{xy} = p^0_{yx}$, the acceptance probability b_{xy} simplifies:

$$b_{xy} = F(\frac{\pi_y}{\pi_x}). \tag{3.23}$$

Now going back to our definition of π_x in (3.15) we can rewrite expression (3.23) as:

$$b_{xy} = F(\exp(-\beta(H(y) - H(x)))). \tag{3.24}$$

As an example, consider the case where we chose a symmetric proposal matrix $p^0_{xy} = p^0_{yx}$ and the function $F(\alpha) = \min(\alpha, 1)$. Then the algorithm simplifies slightly to the following:

1. Generate a proposed move x↦y.

2. If $\beta\triangle H \equiv \beta(H(y) - H(x)) \leq 0$, then the proposed move is accepted with probability 1.

3. If $\beta\triangle H > 0$, then the proposed move is accepted with probability $\exp(-\beta\triangle H)$. In other words, generate a random number γ from the uniform distribution on [0,1], and accept the proposed move if $\gamma \leq \exp(-\beta\triangle H)$, otherwise reject it. When we reject a move we make a null transition, i.e. we count the old configuration as a new configuration.

4. Calculate the necessary averages.

Note that there is nothing special about the proposal matrix P^0 being symmetric; as long as one can compute the ratio $\frac{\pi_y p^0_{yx}}{\pi_x p^0_{xy}}$ the algorithm will work. For more details on how to implement and improve this algorithm see Binder,Heermann [4] and Sokal [55]

3.3.2 Details of the Implementation of the Metropolis Sampling

In this section we give the details of the implementation of the Metropolis sampling designed specifically to compute the ensemble averages with the measure (3.5),(3.6). In the previous section we considered the Hamiltonian without a constraint. Now we are going to add the constraint (3.13) into the algorithm.

Pick some arbitrary initial configuration $(u_1, v_1, \ldots, u_n, v_n)$ that satisfies the constraint (3.13). To generate a new configuration that will satisfy the constraint (3.13) pick some i and j between 1 and n; generate a random number δ uniformly distributed on the interval [0,1], and compute the proposed values of u_i^{new} and v_j^{new} as

$$u_i^{new} = r\cos(2\pi\delta), \qquad v_j^{new} = r\sin(2\pi\delta), \tag{3.25}$$

where $r = \sqrt{u_i^2 + v_j^2}$. Notice that if the proposed move is accepted the constraint (3.13) will be satisfied since $u_i^{new2} + v_j^{new2} = u_i^2 + v_j^2$.

In this construction it is obvious that probability to go from the old configuration to the new configuration is equal to the probability to go from the new configuration to the old configuration; therefore the proposal matrix $P^0 = (p_{xy}^0)$ introduced in the previous section is symmetric, and as mentioned above, the algorithm simplifies a little bit since p_{xy}^0 and p_{yx}^0 cancel out in the ratio (3.22); and we do not need the specific values of p_{xy}^0 and p_{yx}^0 for the method.

We organize the computations in the following way. Fix $i = 1$ and take $j = 1$; generate a new configuration satisfying the constraint (3.13); accept or reject it according to the rule given in the previous section, then take $j = 2$; generate a new configuration and accept or reject it, then take $j = 3$, etc. until $j = n$. After that fix $i = 2$ and let j vary from

1 to n; after that fix $i = 3$, and continue this procedure until $i = n$. It is easy to see that after n^2 steps of this algorithm the probability to get from some arbitrary configuration x to an arbitrary configuration y, satisfying the constraint (3.13) is nonzero; and so the irreducibility condition is satisfied.

The way to organize the computations which we just described is not unique. One can, for example, pick i and j at random, or use another method for generating a new configuration, as long as the irreducibility condition holds.

3.3.3 Numerical Method for Integration of the Schrödinger equation

Now we present a numerical method for integration of the non-linear Schrödinger equation; the method is described in [32]. The idea is to use Strang-type splitting for the linear and nonlinear parts of equations (3.2). In one fractional step solve the linear equation

$$\dot{q} = -p'', \qquad \dot{p} = q''; \tag{3.26}$$

by using discrete fast Fourier transform. As in the previous section, discretize the real and imaginary part of the solution in space on the interval [0,L] by n points as $(u_j,\ v_j)$ respectively, $j = 1, \ldots, n$. Obtain the Fourier modes $(\hat{u}_k, \hat{v}_k)$, $k = 1, \ldots, n$; then apply the exact solution formula

$$\hat{u}(t + \Delta t) + \imath\hat{v}(t + \Delta t) = (\hat{u}(t) + \imath\hat{v}(t)) \exp(-\imath 4[\sin(\frac{\pi k}{n})\frac{n}{L}]^2 \Delta t); \tag{3.27}$$

invert the Fourier transform to return to the physical space. In the second fractional step solve the nonlinear equations

$$\dot{q} = -p(p^2 + q^2), \qquad \dot{p} = q(p^2 + q^2), \tag{3.28}$$

using the formula

$$u_j(t+\Delta t) + \imath v_j(t+\Delta t) = (u_j(t) + \imath v_j(t)) \exp(\imath(u_j(t)^2 + v_j(t)^2)\Delta t). \tag{3.29}$$

In the next step of the numerical algorithm the first fractional step is applied, then the second fractional step, etc. The two fractional steps are alternated to maintain a second order accuracy in time and space. This scheme is unconditionally stable in time for any time step.

This numerical method conserves the discrete constraint (3.13) since each fractional step of the method conserves (3.13). In our computations we monitored conservation of the Hamiltonian and the constraint (3.13) as an accuracy check.

3.4 Comparison of the Time and Ensemble Averages

Now we present numerical evidence for the equivalence of the ensemble (3.5), (3.6) and the microcanonical ensemble; in Figure (3.1) we show the energy fluctuation of the ensemble (3.5), (3.6) around its mean energy, i.e.

$$\frac{< H^2 > - < H >^2}{< H^2 >}, \tag{3.30}$$

computed at some fixed temperature versus the constraint N.

We introduce the energy fluctuation (3.30) into our presentation to estimate the concentration of the measure (3.5),(3.6) on the configurations with the mean energy $< H >$. We argued above in section 3.2 that if the measure (3.5),(3.6) is concentrated on the configurations that belong to the energy shell defined by $< H >$, then it is plausible that the averages with respect to (3.5),(3.6) and the microcanonical ensemble will be the same.

As one can see from the graph in Figure (3.1) the energy fluctuation tends to zero as N increases. This suggests that for large values of N the probability density on the space of configurations is concentrated on the energy shell defined by the mean energy $< H >$.

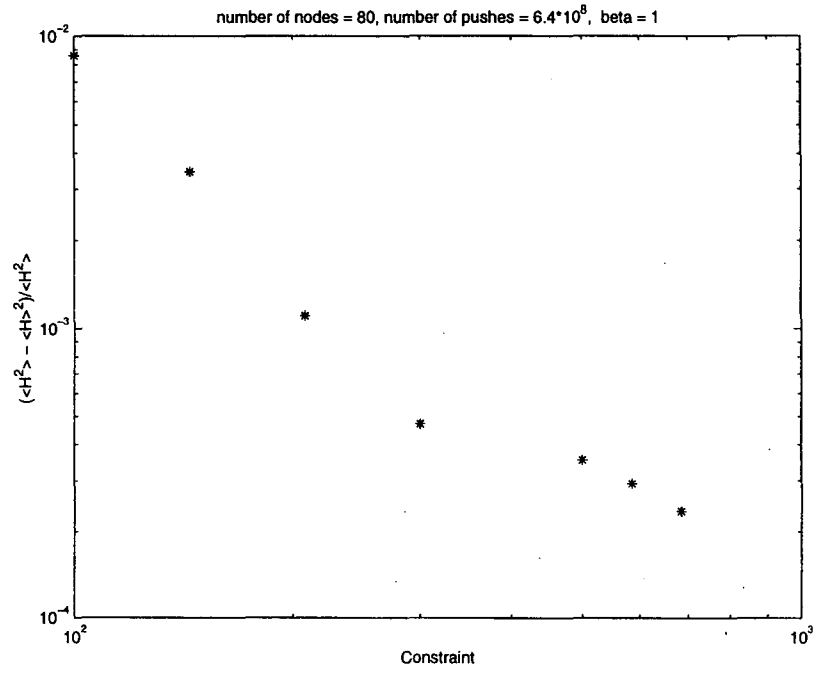

Figure 3.1: Equivalence of the ensemble (3.5), (3.6) and the microcanonical ensemble.

For the dynamical system (3.2) we choose some initial configuration with the energy equal to the average ensemble energy (3.5), (3.6). In Figure (3.2) we present the calculations of the time average and the ensemble average of the following quantity

$$\frac{< \int_0^L (p^2 + q^2)^2 dx >}{N^2}. \tag{3.31}$$

One can see from Figure (3.2) that there is a remarkable agreement between the time and the ensemble average! In this computation the number of discretization points was taken to be 40, and the value of the constraint N (3.13) equal to 10^3. The same agreement was

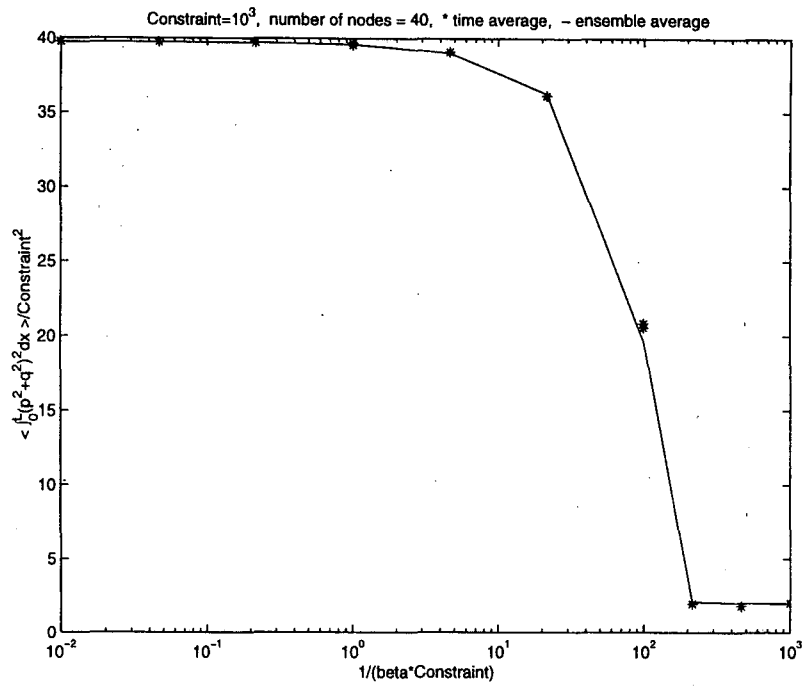

Figure 3.2: Time average and ensemble average

observed when we increased the number of discretization points to 80 and 150, and changed the value of the constraint. Therefore we conjecture that our discrete dynamical system is ergodic. One remark should be made here about the continuum dynamical system. The cubic Schrödinger equation has an infinite family of conserved quantities (see [51]); the numerical scheme that we use to integrate the cubic Schrödinger equation in time does not have a corresponding infinite family of conserved quantities; although we verify the conservation of the Hamiltonian and the constraint N (3.13) in the integration in time. Therefore the trajectory in time of the numerical scheme visits a larger subspace than the actual continuum solution, and the ergodicity that we describe here might be due to the particular numerical algorithm.

Chapter 4

Phase Space Topological Changes and Bifurcation

In this chapter we present numerical results on the bifurcation of the measure (3.12),(3.13) which is directly linked to the phase transition type behavior observed in [41].

4.1 The History of the Problem

In [41] the statistical ensemble for the nonlinear Schrödinger equation (3.5), (3.6) is introduced. In the terminology of [41] the solution of the nonlinear Schrödinger equation ψ is called a complex field; recall that for the cubic Schrödinger equation in Chapter 3 we used the real valued functions q and p for the real and imaginary parts of ψ respectively, i.e.

$$\psi(x) = q(x) + \imath p(x), \tag{4.1}$$

where x is a scalar argument. We are going to refer to the pair of functions (q, p) as a field. It was observed in [41] that there is a large difference between the form of the typical field configuration for low temperatures and the form for high temperatures; for example, in Figure (4.1) we present the typical real and imaginary components of the field for low temperature and large constraint N. These functions look like humps, while for high temperature the typical functions look like random fluctuations; we present high temperature typical functions in Figure (4.2). The word typical here means that the measure is concentrated on the functions similar in shape to the typical ones.

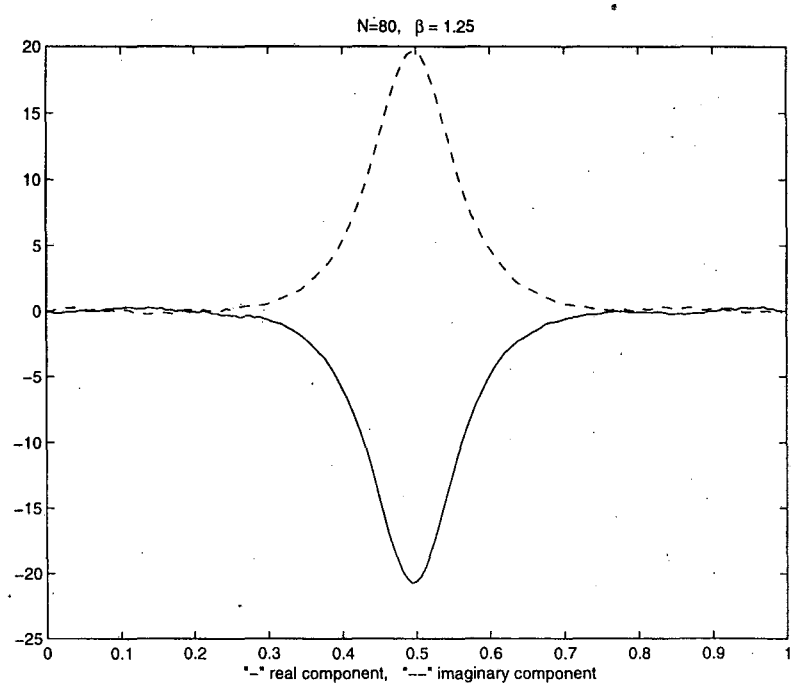

Figure 4.1: Typical real and imaginary components of the field for low temperature and large constraint.

In the next picture we present the typical functions for low temperature and small constraint N. The typical functions here are almost constant up to small random fluctuations.

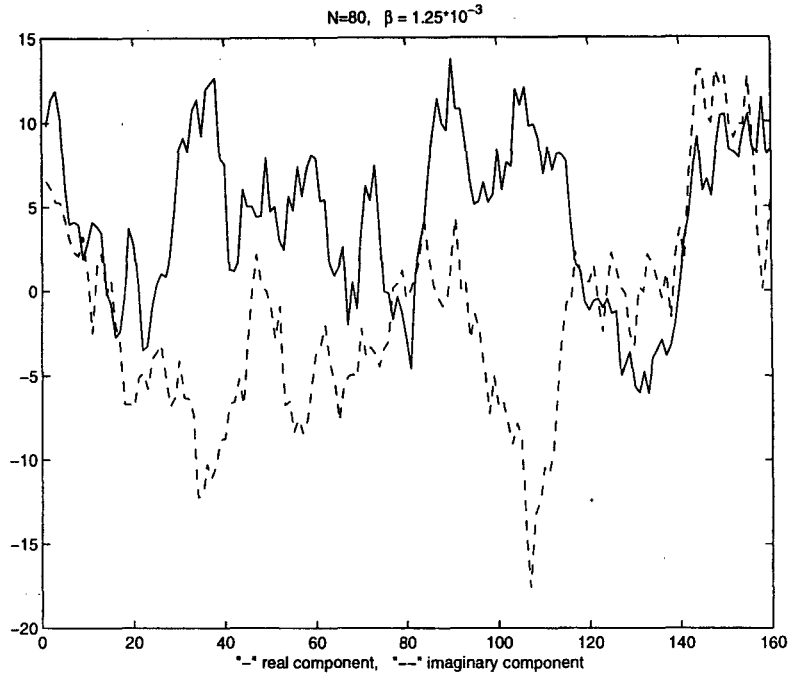

Figure 4.2: Typical real and imaginary components of the field for high temperature.

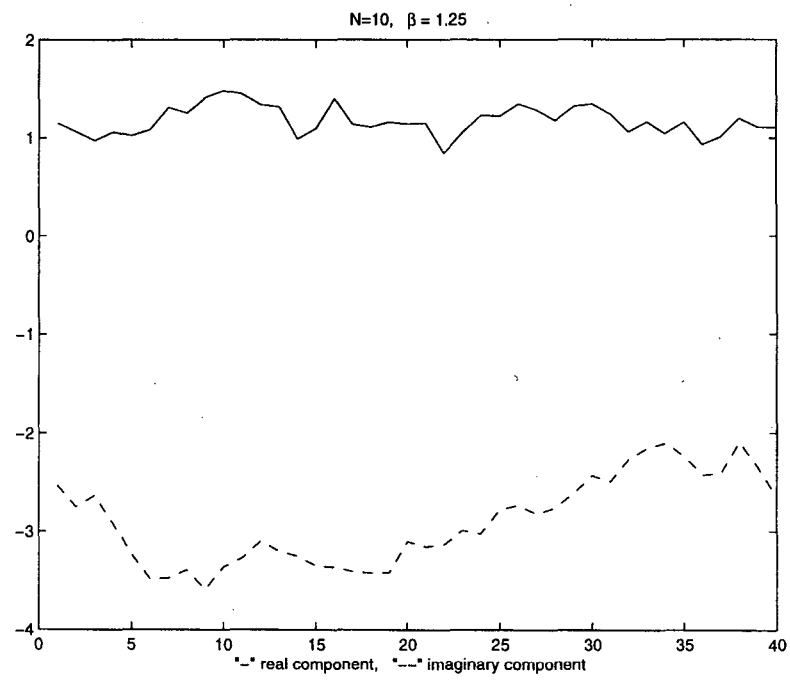

Figure 4.3: Typical real and imaginary components of the field for low temperature and small constraint.

This definition of typical is not very precise, so in order to make the definition more rigorous the following quantity was introduced,

$$S(x) =< q^2(x) + p^2(x) >, \tag{4.2}$$

where <> stands for averaging with respect to the statistical ensemble (3.5), (3.6). The problem with this definition of $S(x)$ is that the Hamiltonian (3.3) is translation invariant on the periodic fields; thus for example if we take the field in Figure (4.4) and translate it in space by any amount, the new field will have exactly the same statistical weight. Suppose for a moment that all the statistical weight of the ensemble (3.5), (3.6) is concentrated on the fields just like the one in Figure (4.4); then simple averaging as defined in formula (4.2) will smear the humps, and the result will be $S(x)$ equal to some constant. In order to make sense of $S(x)$ we have to eliminate the translation invariance. The method used in [41] is the following: for every field (q, p) to find a point x such that $q^2(x) + p^2(x)$ is maximal, and translate the maximum of the field to the middle of the interval $[0, L]$ and then take an average in (4.2).

This translation approach produces an artificial spike in the middle; in order to eliminate this effect it was suggested in [41] to divide $S(x)$ by the quantity

$$S^0(x) =< q^2(x) + p^2(x) >_0, \tag{4.3}$$

where 0 denotes the average with respect to the statistical ensemble (3.5), (3.6) without the potential energy term in the Hamiltonian (3.3).

The quantity $\frac{S(x)}{S^0(x)}$ is plotted in Figure (4.4); the main result of this computation is that the typical field configurations for low temperatures look like sharp spikes (or soliton-like structures as they were referred to in [41]). For high temperatures, the typical field

configurations look like constant functions with oscillations added to them. As one can see, qualitatively the picture remains the same as in Figure 4.1 — sharp spikes are typical for low temperatures, and flat configurations are typical for high temperatures.

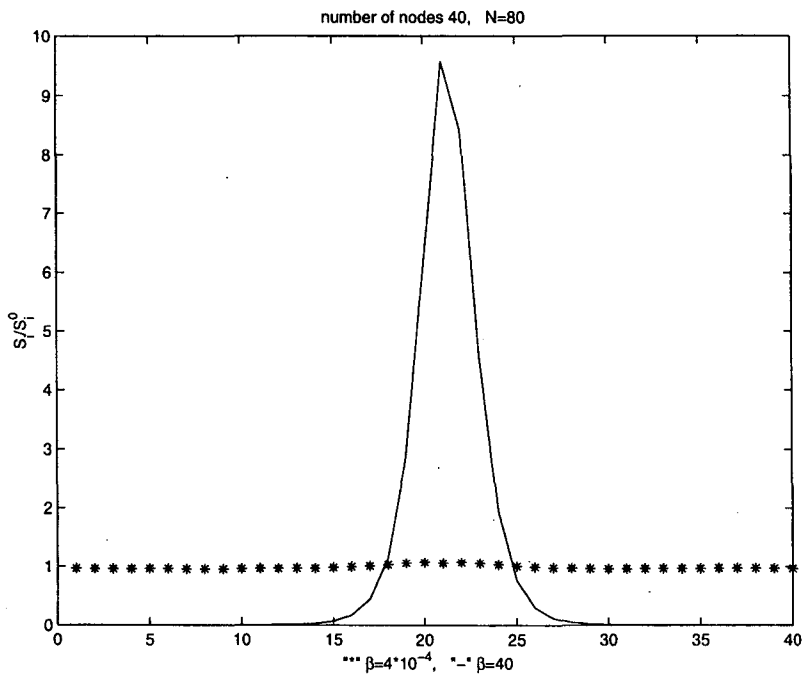

Figure 4.4: Plot of $S(x)/S^0(x)$ for high and low temperatures

Although the pictures 4.4 and 4.1 are intuitively easy to understand, the construction of $\frac{S(x)}{S^0(x)}$ is slightly artificial. Another approach to studying the change in the typical field configurations, which does not involve artificial translation invariance breaking, is to compute the typical kurtosis of the field configurations

$$K = \frac{< \int_0^L (q^2(x) + p^2(x))^2 dx >}{< \int_0^L (q^2(x) + p^2(x)) dx >^2}. \tag{4.4}$$

The denominator in (4.4) is used for the normalization; recall that our measure must satisfy

the constraint (3.6), therefore (4.4) can be rewritten in the form

$$K = \frac{< \int_0^L (q^2(x) + p^2(x))^2 dx >}{N^2}. \tag{4.5}$$

The reason for introducing the quantity K is to distinguish the field configurations that have sharp spikes from those that are flat. We would expect that at low temperatures K would be larger than at high temperatures, provided the constraint (3.6) is large enough. This is indeed what happens, (see Figure (4.5)). One can see that there are two distinctly different regimes in this picture, at low and high temperature, and also a transition region between them.

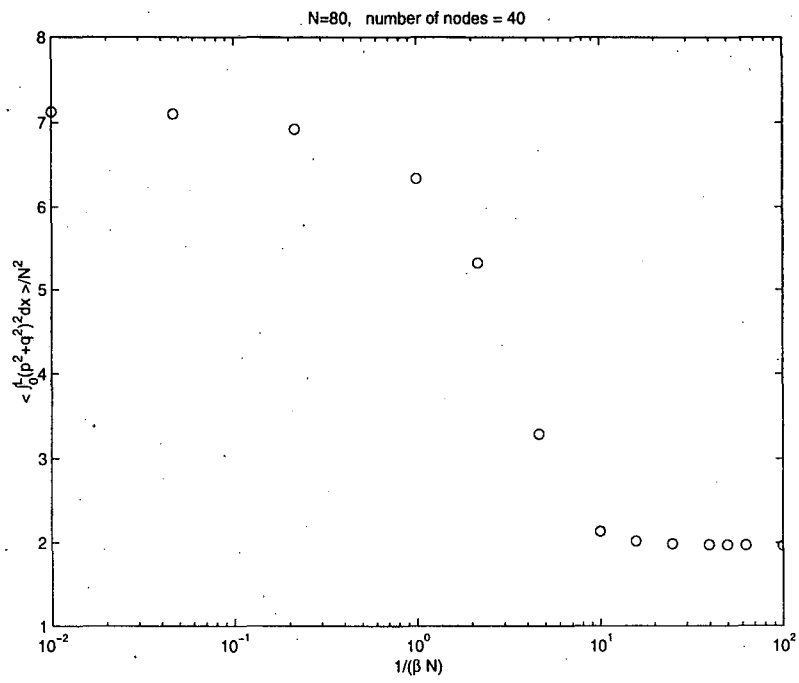

Figure 4.5: Values of K for fixed N=80, and varying β.

The left part of the graph in (4.5) ($10^{-2} \leq \frac{1}{\beta N} < 1$) corresponds to the sharp spike in Figure 4.4, and the right part of the graph ($10 \leq \frac{1}{\beta N} \leq 10^2$) corresponds to the

flat configuration in Figure 4.4.

Let us summarize our observations so far. At low temperatures the kurtosis K of the typical field configurations is high; and it remains almost constant if we increase the temperature up to a certain value. Once the temperature reaches the transition region, K decreases sharply; for higher temperatures K again becomes almost constant.

So far we have discussed the change in the kurtosis (4.5) with respect to temperature. Now we would like to look at the change in the kurtosis when we vary both constraint N and temperature. In Figure 4.6 we present plots of the kurtosis (4.5) for $N = 10, 40, 80$.

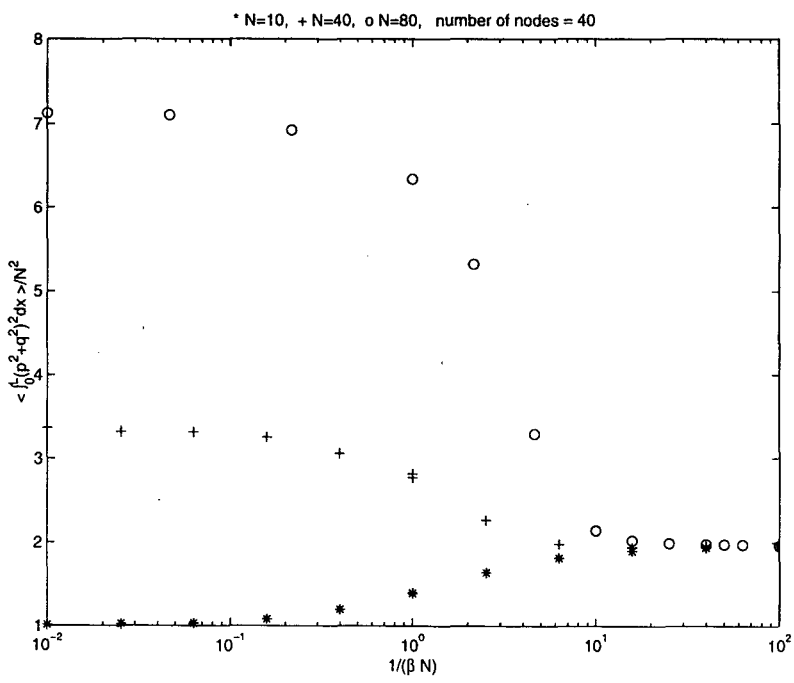

Figure 4.6: Values of K for N= 10, 40, 80 and varying β.

Notice that on the left hand side of the picture in (4.6) ($10^{-2} \leq \frac{1}{\beta N} < 1$) the three curves are distinctly different and almost constant; in the transition region $1 \leq \frac{1}{\beta N} \leq 10$, the curves come together, and for $10 \leq \frac{1}{\beta N} \leq 10^2$ the three curves assume the same constant

value.

This behavior of the kurtosis K is very similar to the pictures of phase transition in statistical physics [28], and it raises the question as to whether this is indeed a phase transition or if some other phenomenon is taking place?

In order to examine this question we start by studying a simplified system, and then moving to a more general one. Before we begin the study of a simple case, we need some definitions.

4.2 Definitions

Suppose we are given a discrete canonical measure (3.12),(3.13), and we want to compute an average with respect to this measure of some quantity using the Metropolis sampling algorithm. We start with some random initial configuration, which we denote by $x_1 \equiv (u(1), \ldots, u(n), v(1), \ldots, v(n))$, and then run the Metropolis sampling, as described in the Chapter 3, for some large number of steps M, storing each configuration as a point x_i, $i = 1, \ldots, M$. After M steps we will get M points, $(x_1, \ldots, x_M)$; this collection of M points we will call a Metropolis sampling trajectory. Notice that this Metropolis sampling trajectory does not depend on a quantity computed in the Metropolis sampling algorithm; it only depends on the temperature in the ensemble and on the initial point.

The Metropolis sampling trajectory is a trajectory in 2n-dimensional space; we can define a projection of the Metropolis sampling trajectory onto a 3-dimensional subspace by picking any three components of the vectors u,v, for example u_1, u_2, v_3. In a similar way we can define a projection of a Metropolis sampling trajectory onto a three dimensional

subspace, which we will denote by $(x_1^p, ..., x_M^p)$.

Now consider a time dependent Hamiltonian system with periodic boundary conditions (3.2); discretize this system in space by n points, and integrate it in time for some large time T, starting at some initial configuration $y_1 \equiv (u(1), \ldots, u(n), v(1), \ldots, v(n))$. For integration in time we use some numerical method, for example the one described in Chapter 3; we define the time trajectory as a collection of points $(y_1, \ldots, y_K)$, $K\Delta t = T$, where Δt is the time step of the numerical integration scheme. The time trajectory is a trajectory in 2n-dimensional space, and $(y_1^p, \ldots, y_K^p)$ is the projection of the time trajectory onto a three-dimensional subspace, which we will call a projected time trajectory.

4.3 Simple case

To motivate the discussion later in this chapter we consider a very simple discrete periodic in space system (3.11),(3.13) with just 2 discretization points, i.e. in (3.11), (3.13) we take $n = 2$, or explicitly the Hamiltonian is given by

$$H = \frac{1}{2}\sum_{i=1}^{2}((\frac{u_{i+1} - u_i}{h})^2 + (\frac{v_{i+1} - v_i}{h})^2)h - \frac{1}{4}\sum_{i=1}^{2}(u_i^2 + v_i^2)^2 h, \tag{4.6}$$

which leads to the following discretization of the measure (3.5), (3.6)

$$\mathbf{P}(du, dv) = Z_2^{-1} \exp[-\beta\frac{1}{2}\sum_{i=1}^{2}((\frac{u_{i+1} - u_i}{h})^2 + (\frac{v_{i+1} - v_i}{h})^2)h - \frac{1}{4}\sum_{i=1}^{2}(u_i^2 + v_i^2)^2 h]dudv, \tag{4.7}$$

and

$$N = \sum_{i=1}^{2}(u_i^2 + v_i^2)h, \tag{4.8}$$

where h = $\frac{L}{2}$ is the discretization step. The equations of motion can be written as:

$$\dot{u_i} = -\frac{v_{i+1} - 2v_i + v_{i-1}}{h^2} - v_i({u_i}^2 + {v_i}^2), \qquad \dot{v_i} = \frac{u_{i+1} - 2u_i + u_{i-1}}{h^2} + u_i({u_i}^2 + {v_i}^2), \tag{4.9}$$

where i=1,2; and since u and v are periodic by definition $u_3 \equiv u_1$, $u_0 \equiv u_2$, $v_3 \equiv v_1$, and $v_0 \equiv v_2$.

The reason for choosing such a system is its simplicity; we can visualize this system in 3-dimensional space, because this system is almost 3-dimensional. By almost 3-dimensional we mean that given three arbitrary components of the system, for example u_1, u_2, and v_1, one can determine v_2 from (4.8) up to a sign.

Now we investigate the phase space of the dynamical system (4.9); we start the system at various initial conditions with different values of the Hamiltonian (4.6) and the fixed value of the constraint (4.8) and follow the system for large enough time, so that the system settles into some periodic or quasiperiodic motion.

4.3.1 Phase space splitting of the dynamical system into energy level sets

We begin by fixing some value of the constraint (4.8) and pick the initial condition corresponding to the minimum value of the Hamiltonian (4.6). In Figure (4.7) we plot the time trajectory that corresponds to the minimum value of the Hamiltonian. This time trajectory corresponding to the minimum of the Hamiltonian lies in a plane, which we call a minimum energy plane. We then increase the Hamiltonian and integrate in time starting at some arbitrary initial condition; after some time the time trajectory settles to some quasi periodic motion, which looks like a motion on a surface of a torus (see Figure 4.7).

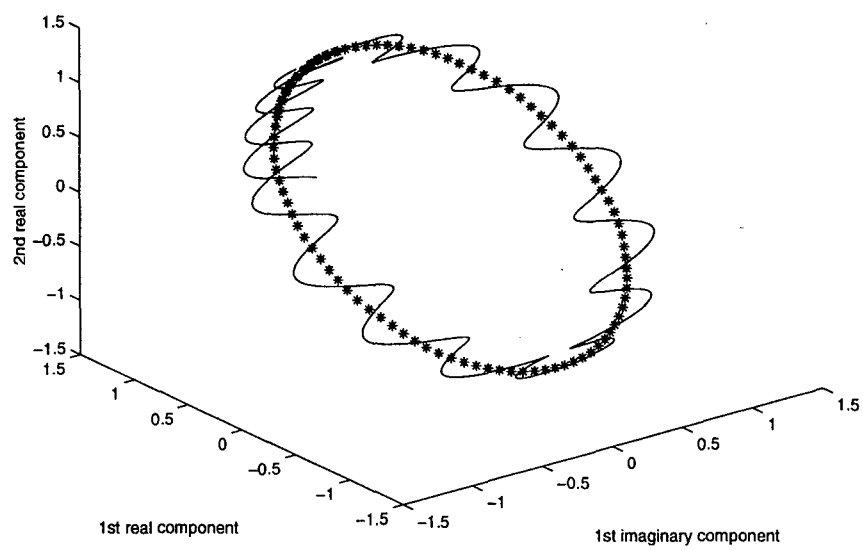

Figure 4.7: Time trajectories in the phase space of the 4-dimensional system with constraint. The axes correspond to the two real components and one of the imaginary components of the system. The thick line corresponds to the minimum value of the Hamiltonian. The thin line corresponds to a value of the Hamiltonian larger than the minimum.

Keeping the value of the constraint (4.8) fixed, we increase the value of the Hamiltonian further; the new time trajectory is plotted in Figure (4.8).

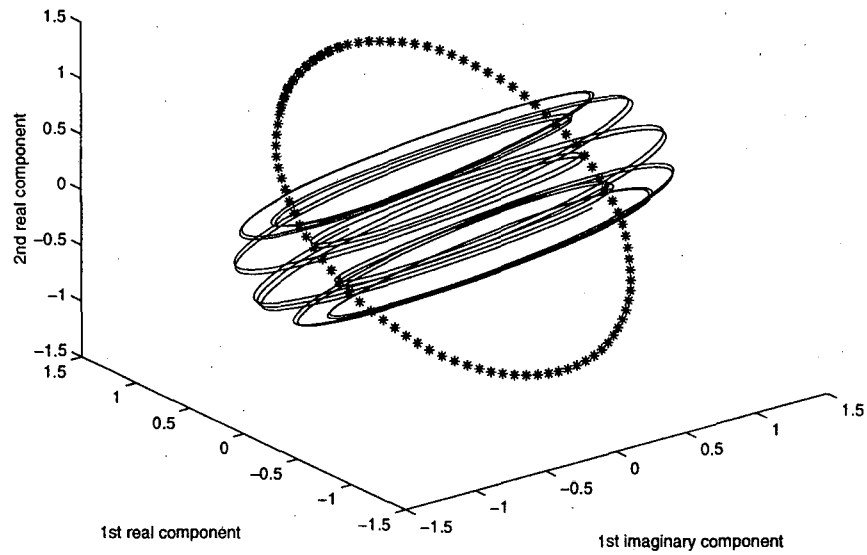

Figure 4.8: Trajectories in the phase space of the 4-dimensional system with constraint. The axes correspond to the two real components and one of the imaginary components of the system. The thick line in this picture is the same minimum energy line as in the figure (4.7) above, and is reproduced in this picture as a reference line.

If we increase the Hamiltonian value even further, and compute the corresponding trajectories, we find that the trajectories collapse onto the line perpendicular to the minimum energy plane (see Figure (4.8)). Finally, at the highest value of the Hamiltonian the trajectory in Figure (4.9) is a circular line in the plane perpendicular to the minimum energy plane.

Figures (4.7)-(4.9) provide a picture of the phase space splitting into various energy surfaces from the minimum to the maximum value of the Hamiltonian with some fixed value of the constraint.

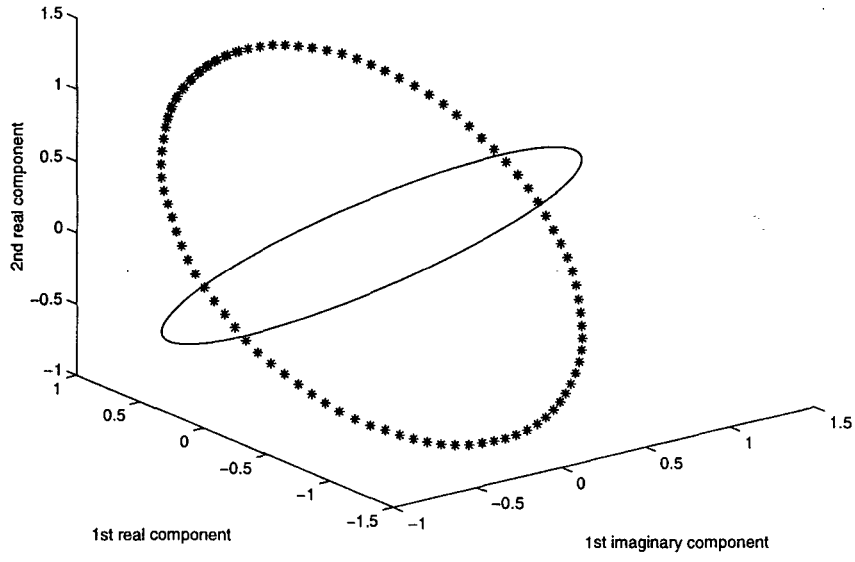

Figure 4.9: Trajectories in the phase space of the 4-dimensional system with constraint. The axes correspond to the two real components and one of the imaginary components of the system. Thick line corresponds to the minimum of the Hamiltonian, and thin line corresponds to the maximum of the Hamiltonian.

4.3.2 Changes of Metropolis sampling trajectories with respect to temperature

Now we would like to find out if there is any connection between the time trajectories of the dynamical system (4.9) and the Metropolis sampling trajectories of the system (4.6), (4.8). Our previous discussion in Chapter 3 suggests that for large inverse temperature β, the configurations that contribute the most to the statistical sum would be concentrated on configurations of minimum energy. This is indeed the case, and we verify this in Figure (4.10), where we plot a Metropolis sampling trajectory for the low temperature with the same value of the constraint (4.8), which we used for the time trajectories above. We started the Metropolis sampling at many different points and each time got the same torus like picture in Figure (4.10).

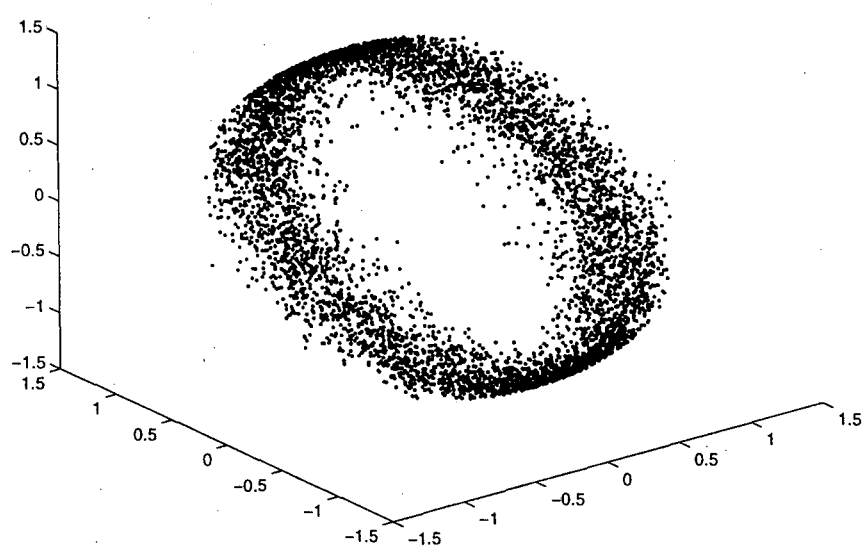

Figure 4.10: Metropolis sampling trajectory of the 4-dimensional system, β=4. The axes correspond to the two real components and one of the imaginary components of the system.

Now we would like to find out how this Metropolis sampling trajectory changes as we increase the temperature. We pick some high enough value of temperature, and compute the Metropolis sampling trajectories starting at various initial configurations. What we see is that the torus-like structure of the most important configurations changes completely and starts to look like a ball.

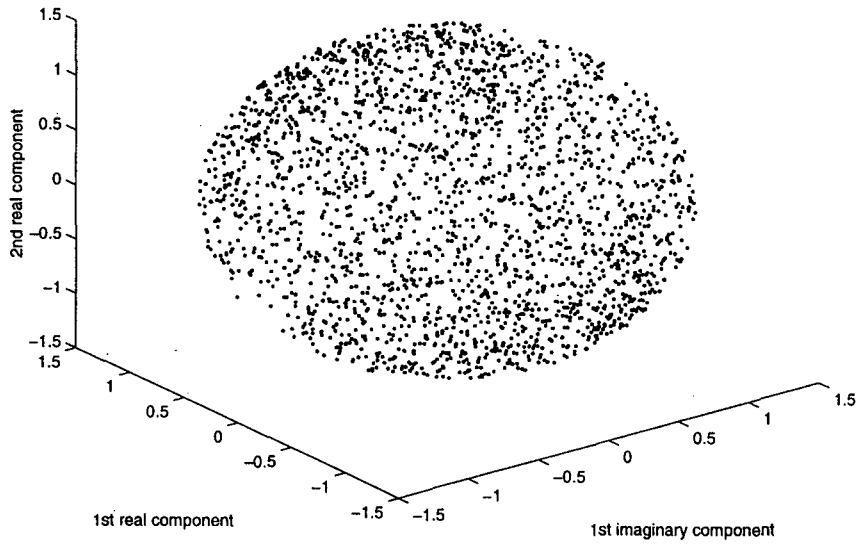

Figure 4.11: Metropolis sampling trajectories of the 4-dimensional system with constraint, β=0.04. The axes correspond to the two real components and one of the imaginary components of the system.

We observe that the typical phase space Metropolis sampling pattern completely changes its topology over some range of values of temperature. In other words, there is a low temperature pattern - a torus, a high temperature pattern - a ball, and a transition region between them, in which torus is transformed into a ball, or vice versa.

Although one specific configuration can be sampled several times and so it will

have a bigger statistical weight associated with it, in Figures 4.10,4.11 such a configuration is shown as just one point. To give a better picture we show the weight of each different energy state in Figures (4.12) and (4.13).

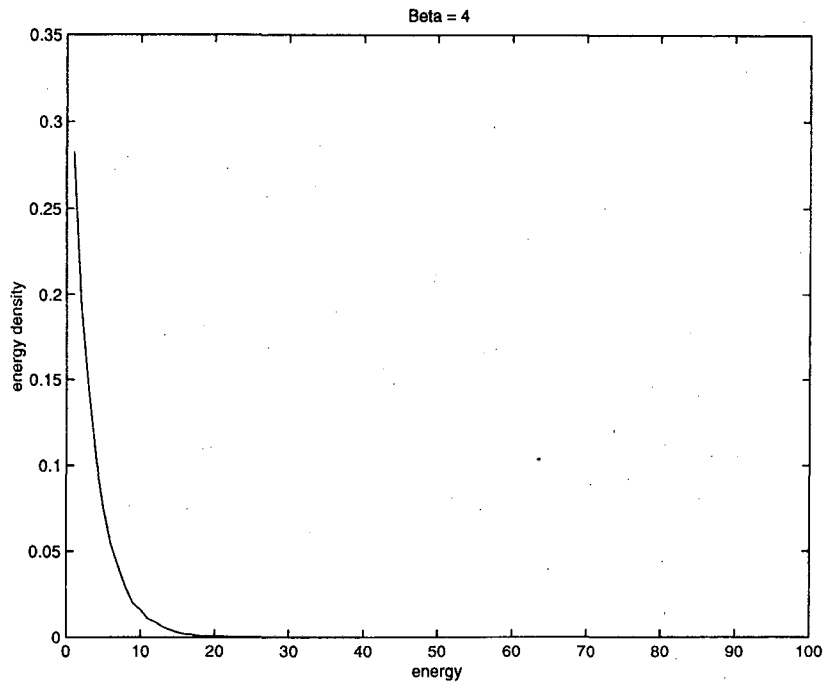

Figure 4.12: Density of states for the Metropolis sampling trajectories. The horizontal axis is the energy, from smallest to largest possible values. The vertical axis is the density of the configuration with each energy.

These pictures show that for low temperature almost all of the contribution to the statistical sum comes from the neighborhood of the smallest energy configuration. An increase in temperature results in a bigger contribution to the sum from the higher energy states, which corresponds to the torus like Metropolis sampling trajectory turning into a ball.

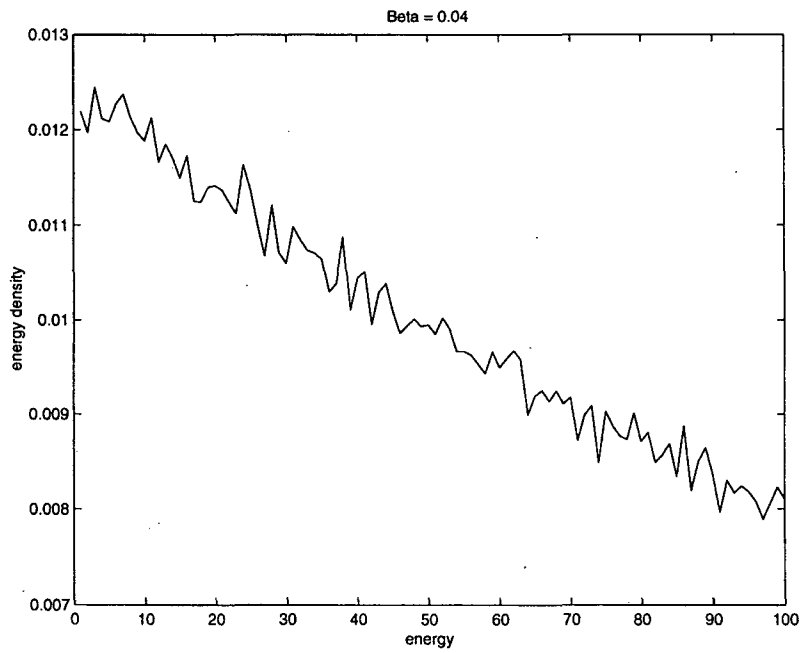

Figure 4.13: Density of states for the Metropolis sampling trajectories. The horizontal axis is the energy, from smallest to largest possible values. The vertical axis is the density of the configuration with each energy.

4.3.3 Changes of Metropolis sampling trajectories with respect to constraint N

So far we have observed that there is a change in the topology of the sample trajectories from a torus to a ball when the temperature is changed. Motivated by this observation, we would like to find out what topological changes happen when we change both the constraint N and the temperature, as in Figure (4.6). First, in Figure (4.14) we present the graphs of K vs. $\frac{1}{\beta N}$ for several different values of N.

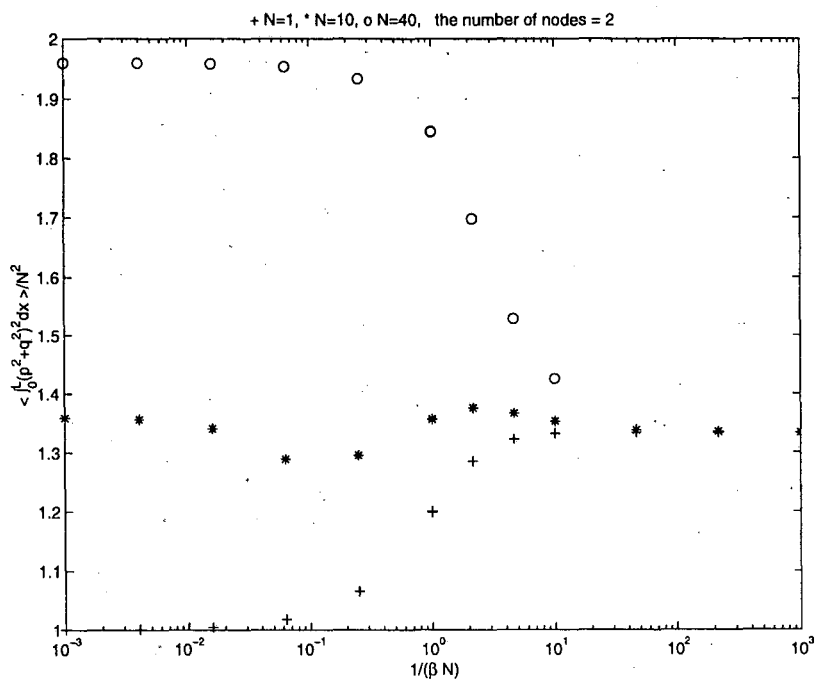

Figure 4.14: Values of K for N= 1, 10, 40 and varying β.

Notice that even for the simple 2 node system there is qualitative similarity between these graphs and the ones in Figure (4.6) for the 40 node system. This indicates that studying a simple 2 node system will provide an insight into the behavior of a more

complicated one.

In Figure (4.14) as in Figure (4.6) there are clearly three distinct regimes; for $10^{-3} \leq \frac{1}{\beta N} \leq 10^{-1}$ the curves corresponding to different constraints are clearly distinct and almost constant; for $10^{-1} \leq \frac{1}{\beta N} \leq 1$ the curves come together, and for $1 \leq \frac{1}{\beta N}$ the curves are indistinguishable and constant.

We would like to find out what are the topological changes in Metropolis sampling trajectories corresponding to the low value of $\frac{1}{\beta N}$ when the three curves in Figure (4.6) are distinct. To do this we fix $\frac{1}{\beta N} = 10^{-2}$ and plot Metropolis sampling trajectories in Figures (4.15), (4.16), and (4.17), for N=1, 10, and 40 respectively.

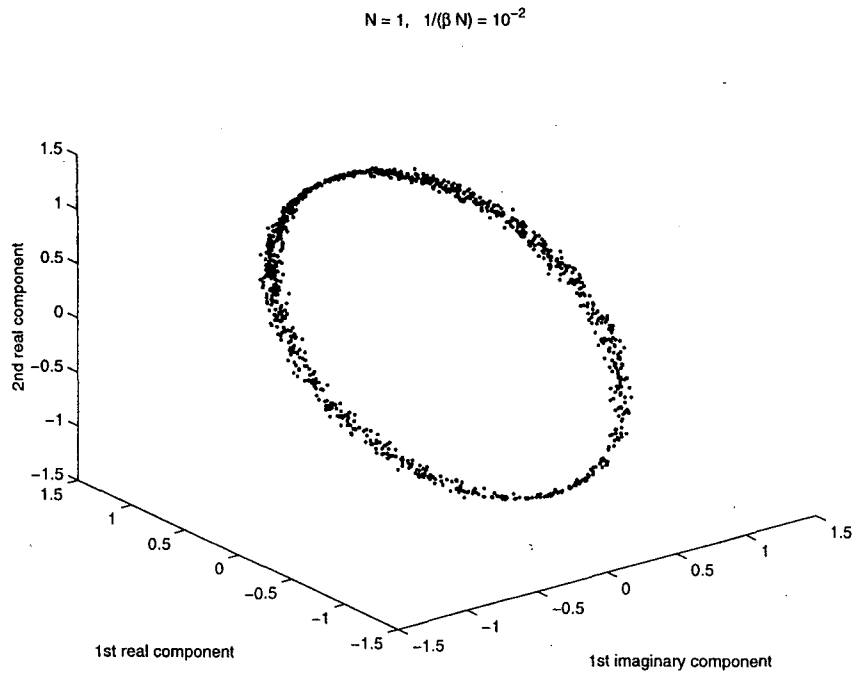

Figure 4.15: Metropolis sampling trajectories of the 2 node system, $N = 1$, $1/(\beta N) = 10^{-2}$.

A new interesting feature has appeared in Figure (4.16) as we increase the value of the constraint N from 1 to 10 — a single torus splits into two tori, and the two tori then

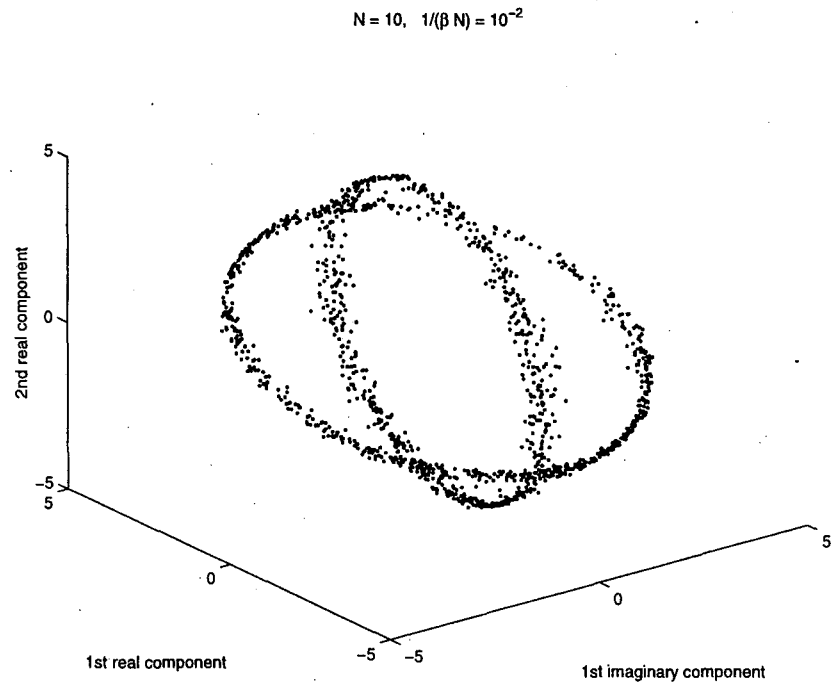

Figure 4.16: Metropolis sampling trajectories of the 2 node system, $N = 10, 1/(\beta N) = 10^{-2}$.

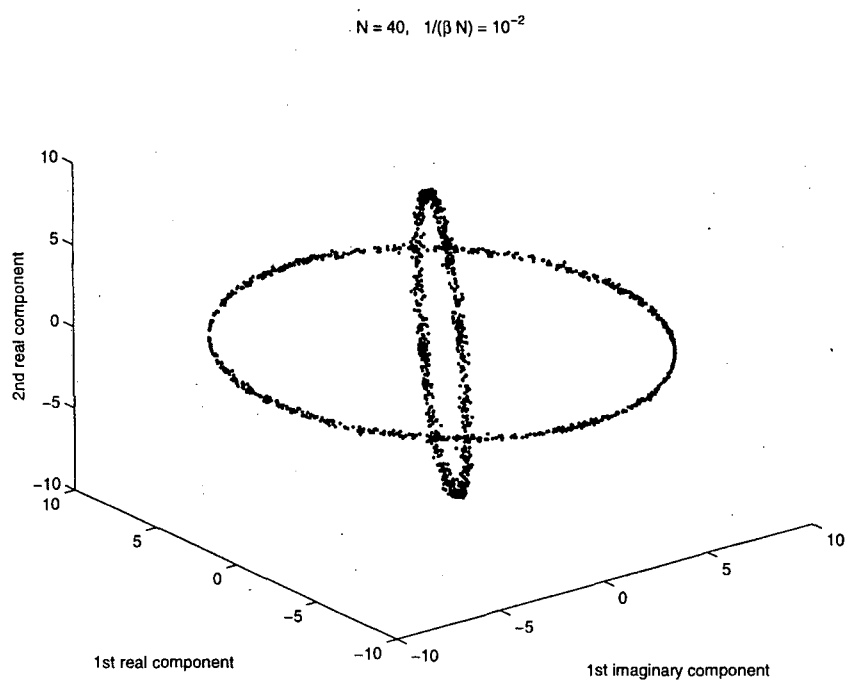

Figure 4.17: Metropolis sampling trajectories of the 2 node system, $N = 40, 1/(\beta N) = 10^{-2}$.

move apart as N increases until they become perpendicular to each other.

In order to see what happens to the two tori Metropolis sampling trajectories ($N = 40$) as we increase the temperature, we pick the first value of β in the transition region, for example $\frac{1}{\beta N} = 1$, and the second value of β in the region where all three curves in Figure (4.14) come together, for example $\frac{1}{\beta N} = 10$. The Metropolis sampling trajectories are shown in Figures (4.18), and (4.19).

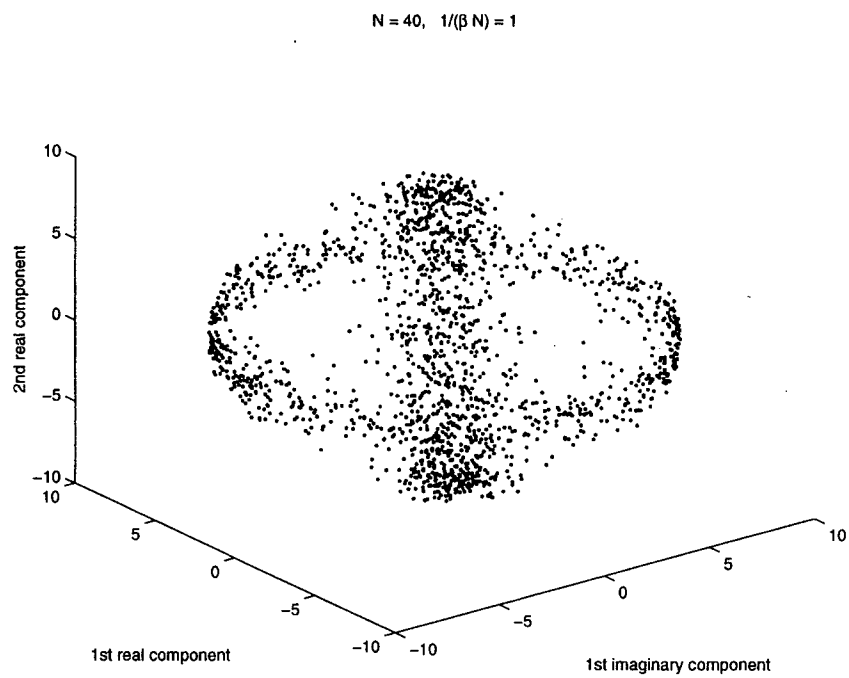

Figure 4.18: Metropolis sampling trajectories of the 2 node system, $N = 40$, $1/(\beta N) = 1$.

One can see from these pictures that as temperature increases the two tori become 'fatter' in the transition region, and turn into a ball for high enough temperatures.

In section 4.3.2 we showed that for low temperatures the Metropolis sampling trajectories are concentrated around the minimum energy time trajectories (see Figures (4.7), and (4.10)); now we present minimum energy time trajectories for $N = 10$, (Figure

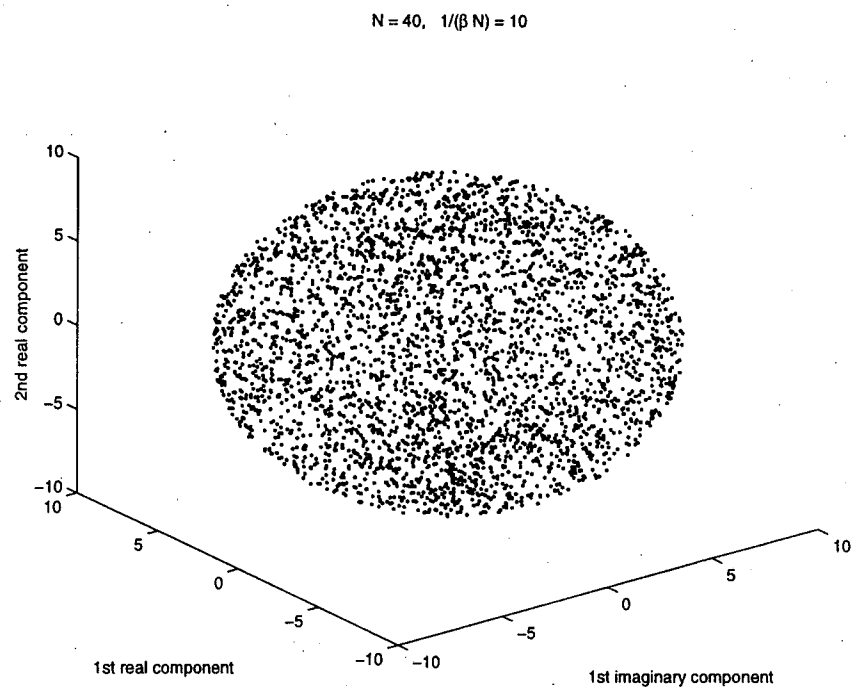

Figure 4.19: Metropolis sampling trajectories of the 2 node system, $N = 40$, $1/(\beta N) = 10$.

(4.20)), and for $N = 40$ (Figure (4.21)).

Recall that there are two time trajectories coming through each point of the phase space, since the fourth degree of freedom of the system is determined from the three shown in the picture and a constraint up to a plus or a minus sign.

If we compare Figures (4.20), (4.21) and Figures (4.16),(4.17) respectively, we again see a very good agreement between Metropolis sampling and time trajectories; this confirms our intuitive reasoning in Chapter 3.

4.4 General case

Now we consider the more general case of the statistical ensemble (3.11),(3.13), and a dynamical system (3.2) with the number of discretization points n greater than 2. We

Figure 4.20: Splitting of the minimum energy circle in the time dependent system, $N = 10$.

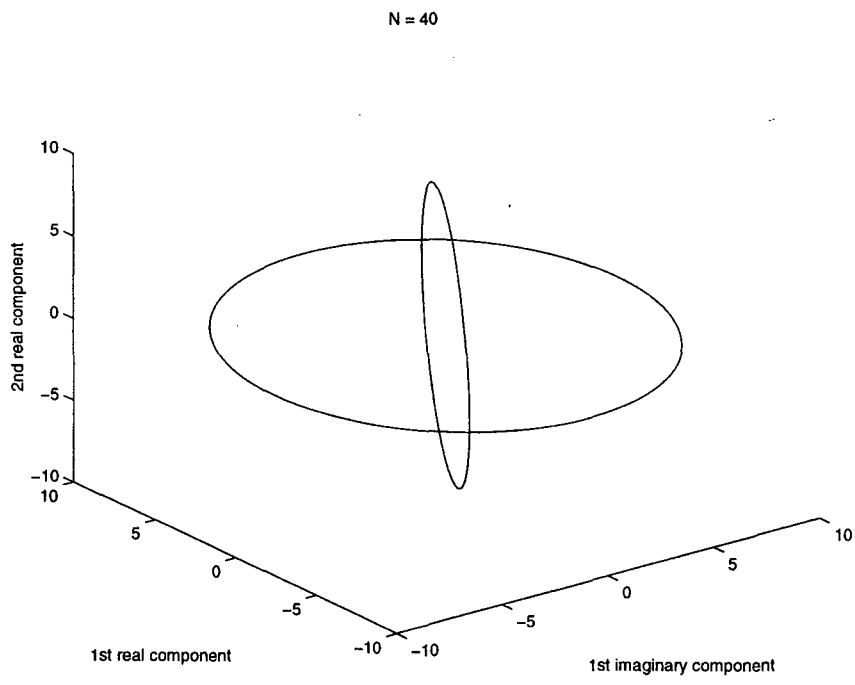

Figure 4.21: Splitting of the minimum energy circle in the time dependent system, $N = 40$.

would like to investigate the connection between changes in kurtosis (4.6) and Metropolis sampling trajectories; we are motivated by the simple 2 point system case of the preceding section, and would like to see whether such phenomena as tori turning into a ball persists for the large system. Since we cannot visualize the whole n-point system as we could before, we have to take projections onto a three-dimensional subspace.

4.4.1 Changes of Metropolis sampling trajectories with respect to temperature in large system.

Surprisingly, we are still able to observe very clearly phase space changes of the Metropolis sampling trajectories at low and high temperatures, which look very much the same as in the simple 2-point case.

We present a typical picture that we observed over different combinations of any three discretization nodes. We picked at random three particular nodes and monitored their Metropolis sampling trajectories for a few different runs of Metropolis algorithm.

In Figure (4.22) we present the projection of the Metropolis sampling trajectory of a 10-point system for low temperature. The parameter range of this system ($N = 1$, $\beta = 4$) corresponds in Figure (4.6) to the left part of the lower curve ($\frac{1}{\beta N} = 0.25$). Notice that the Metropolis sampling trajectory is a single torus and looks very much the same as the torus of the 2-point system in Figure (4.10).

Both of these tori in Figures (4.22), and (4.10) correspond to the lower kurtosis curves in Figures (4.6), and (4.14) respectively.

In the 2-point case we observe that as we increase the temperature the torus like picture turns into a ball. Now we increase the temperature in the large system ($\frac{1}{\beta N} = 10$,

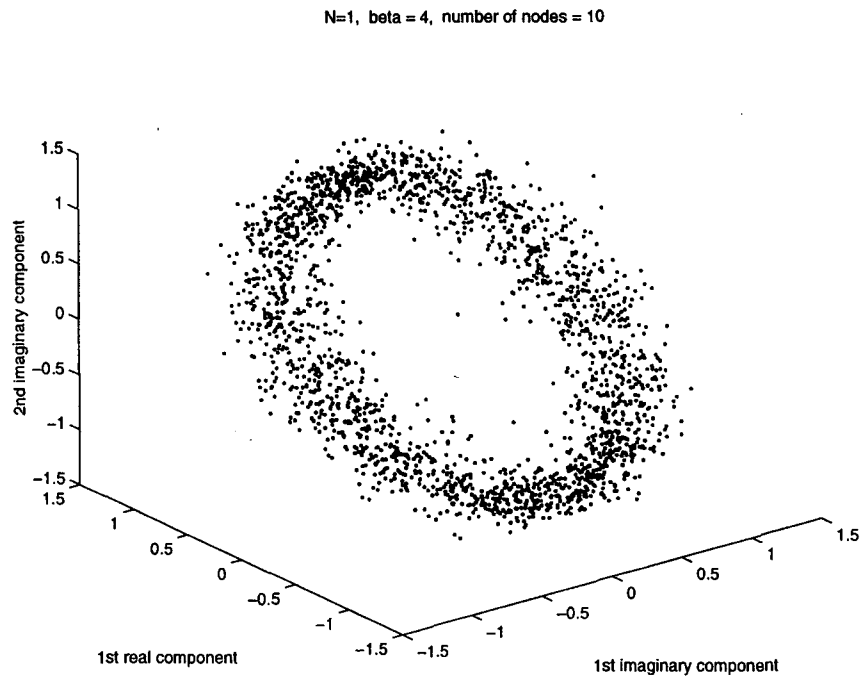

Figure 4.22: Metropolis sampling trajectory for the 10-point system, N=1, $\beta = 4$.

see Figure 4.6) and plot the resulting Metropolis sampling trajectories in Figure (4.23).

Observe that the torus turns into a ball, just as in the 2-point system (see Figures (4.10),(4.11)). This is very surprising; even though the phase space of the larger system is very complicated, the simple phase space structure of the Metropolis sampling trajectories is preserved in the large system.

Let us consider the dynamical system (3.2); which we discretize with a large number of points and integrate in time at a minimum value of the Hamiltonian; the resulting trajectory is given in Figure (4.24).

Notice that, as before in the 2-point case, the Metropolis sampling trajectories for low temperature (Figure 4.22) are concentrated around the energy minimum shown in Figure (4.24).

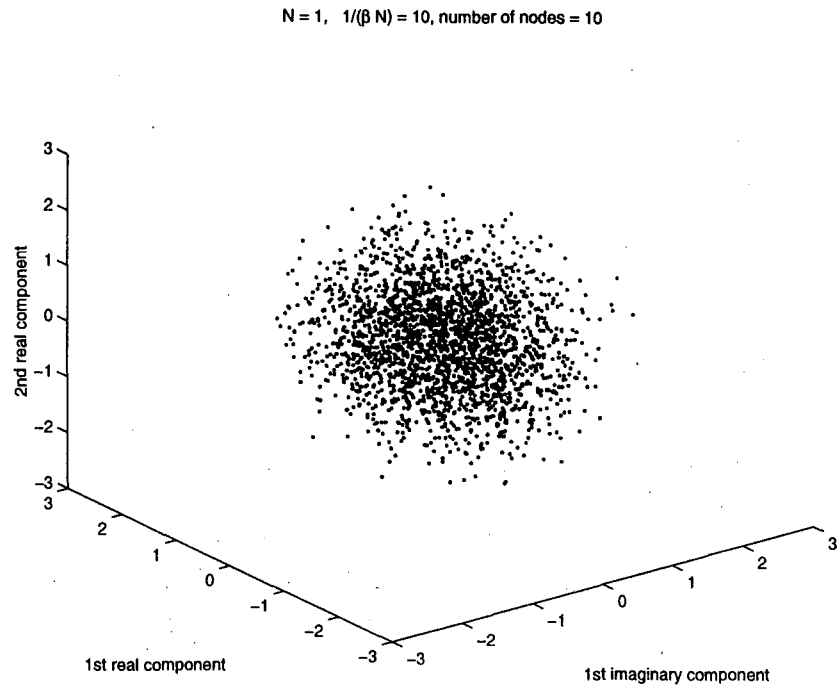

Figure 4.23: Metropolis sampling trajectory for the 10-point system, N=1, $\beta = 0.1$.

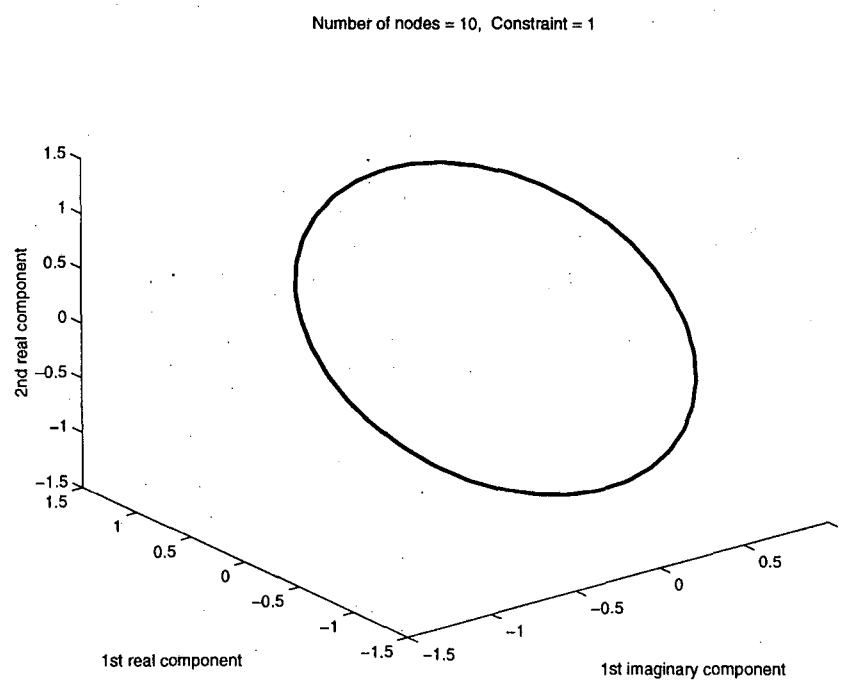

Figure 4.24: Projected time trajectory of the 10-point system for small energy.

4.4.2 Changes of Metropolis sampling trajectories with respect to constraint N in large system

Recall that in Figure (4.6) kurtosis changes depending on both temperature and constraint N. In simple 2-node system we observed that as N increases at low temperature, the torus splitted into two tori (Figures 4.15, 4.16, 4.17). The sample trajectories of the large system also change from a torus to a more complicated structure, which we plot in Figure (4.25); nevertheless the torus like picture splits into something very similar to the two tori picture of the simple 2-point system (see Figure 4.17).

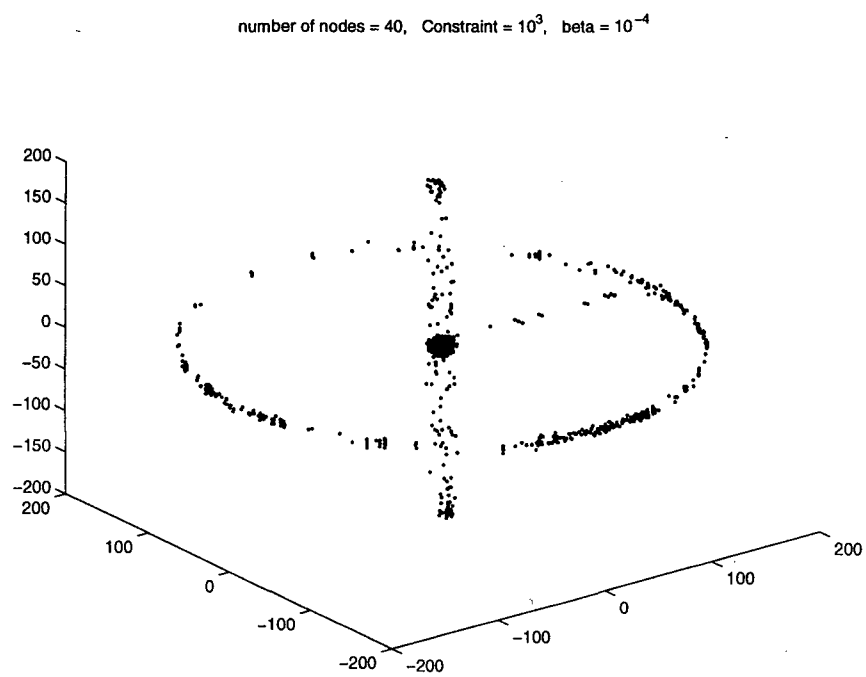

Figure 4.25: Metropolis sampling trajectory for the 40-point system $N = 10^3$, $\beta = 10^{-4}$.

As temperature increases, something similar to the 2-point case takes place; at first the tori structure becomes 'fatter' (see Figure 4.26) and then for high temperature it

turns into a ball (Figure 4.27).

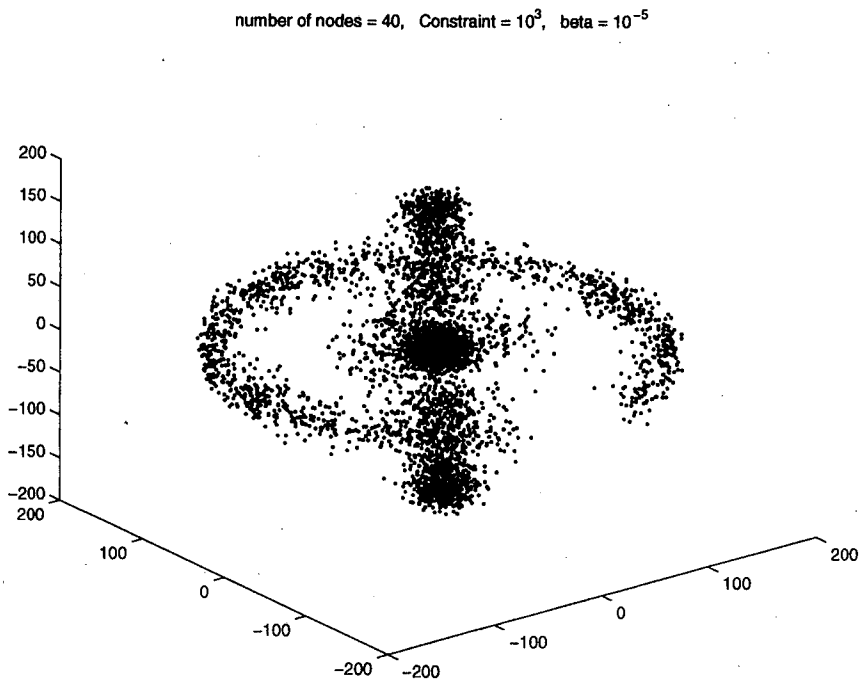

Figure 4.26: Metropolis sampling trajectory for the 40-point system $N = 10^3$, $\beta = 10^{-5}$

Clearly, there is a strong connection between phase space Metropolis sampling trajectories structure and differences in kurtosis (Figure 4.6), which appears in the small 2-node system and persists for larger systems.

4.4.3 Changes in kurtosis K as constraint N increases

It might appear that as N increases for low temperature the kurtosis curves in (Figure 4.6) will tend to a discontinuous step function. However, what really happens for a fixed number of discretization points is that for large enough value of N the curves converge to a smooth function; the results are shown in Figure (4.28).

For values of $N > 640$ presented in Figure (4.28) the curves converge to a curve

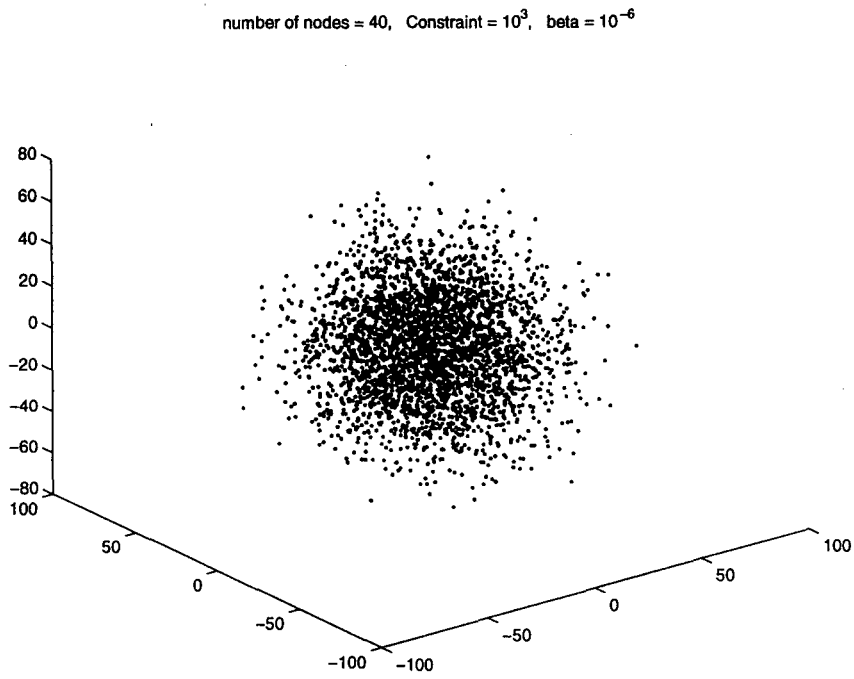

Figure 4.27: Metropolis sampling trajectory for the 40-point system $N = 10^3$, $\beta = 10^{-6}$

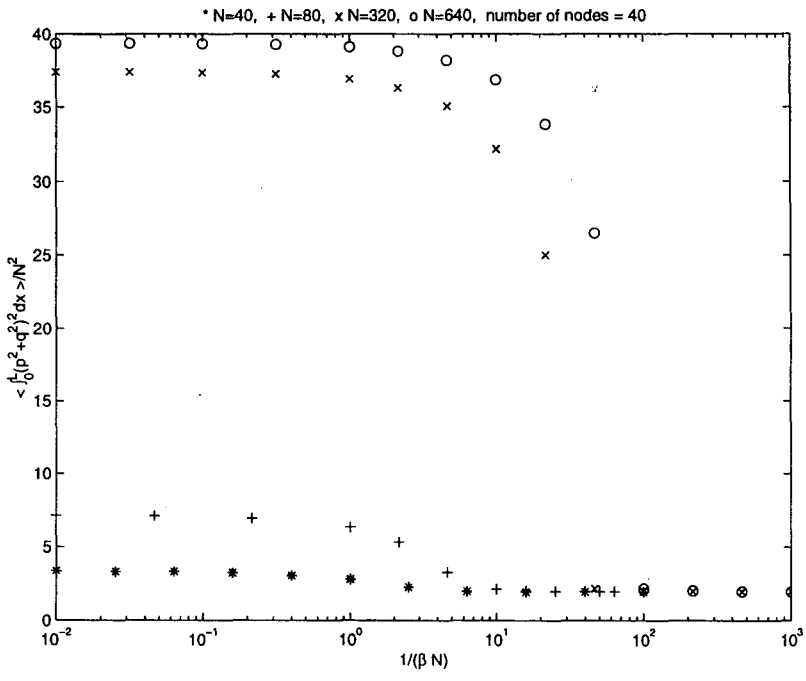

Figure 4.28: Values of K for various N and β

close to the one that corresponds to $N = 640$. From these pictures for the fixed number of nodes we do not observe convergence to the discontinuous step function as N increases.

4.4.4 Changes in kurtosis K as the number of discretization points increases

Now consider the limit in which the constraint N is fixed and the number of discretization points increases. In this case again we observe that the functions converge to some smooth limit function; the results are shown in Figure (4.29).

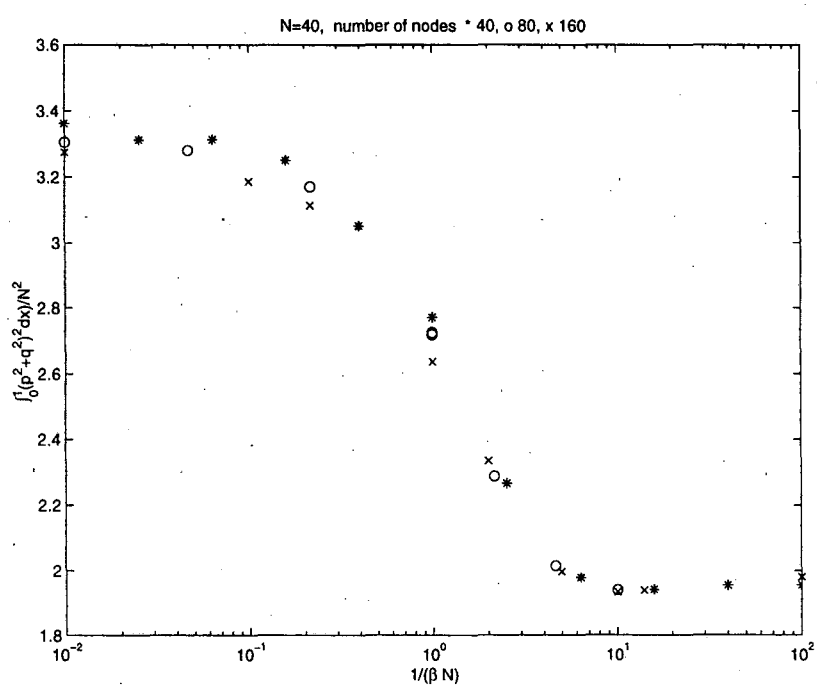

Figure 4.29: Values of K for N=40 and different number of discretization points.

If we pick a larger value of N and compute kurtosis for increasing numbers of discretization points, the functions again converge to some smooth limit function; the results are shown in Figure (4.30).

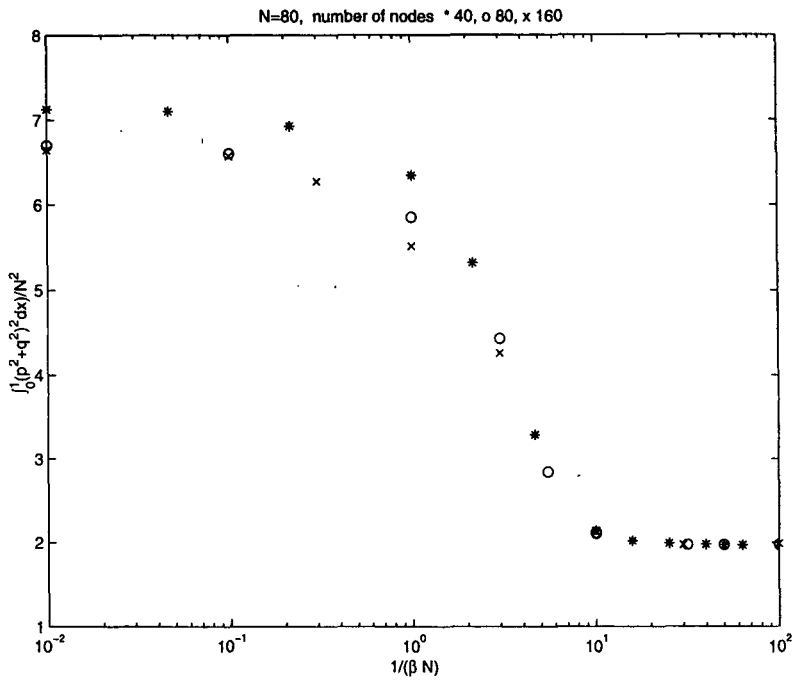

Figure 4.30: Values of K for N=80 and different number of discretization points.

These plots suggests that for a fixed value of N, as the number of discretization points increases the kurtosis converges to a smooth function. However, for larger value of N the kurtosis has a steeper slope in the transition region; this suggests that we need to investigate the limit as both N and the number of discretization points increase.

4.4.5 Changes in kurtosis K as both N and the number of discretization points increase

We are going to show that as we increase the number of discretization points the kurtosis tends towards to a higher limit.

In the previous plots we either used a fixed number of discretization nodes (n=40) or a fixed constraint (N=40, N=80). If we now increase the number of discretization points

and the constraint N simultaneously, we observe that in the transition region the slope of the curve corresponding to larger N is steeper than for a smaller N. If we double the number of nodes, the derivative increases substantially (see the summary in Table (4.1)). This might suggest the possibility of a discontinuity in the function K in the limit as N and the number of discretization points approach infinity. The estimates for the derivatives in the transition region are summarized in Table (4.1).

Number of nodes	Maximum absolute value of the derivative
40	2.1
80	14.1
160	22
320	30.5

Table 4.1: Maximum absolute value of the derivative

The plots of the curves in the transition region are given in Figure (4.31). Here we plot K for increasing number of nodes and increasing values of N. Notice that in Figures (4.28), (4.29, (4.30) we used a logarithmic scale, but we do not use it in Figure (4.31).

Also observe that the horizontal axis in Figure (4.31) is scaled as $\frac{1}{\beta N}$, and as N goes to infinity the transition region increases which implies that the temperature in the transition region goes to infinity.

To summarize: In the transition region between low and high temperatures the slope of K increases in absolute value as the number of nodes and the constraint N increase. However, the numerical simulation cannot provide a proof that there is a discontinuity in the limit as the number of discretization nodes and N go to infinity. Investigating numerically a system of more than 500 discretization nodes or 1000 degrees of freedom (500 real and

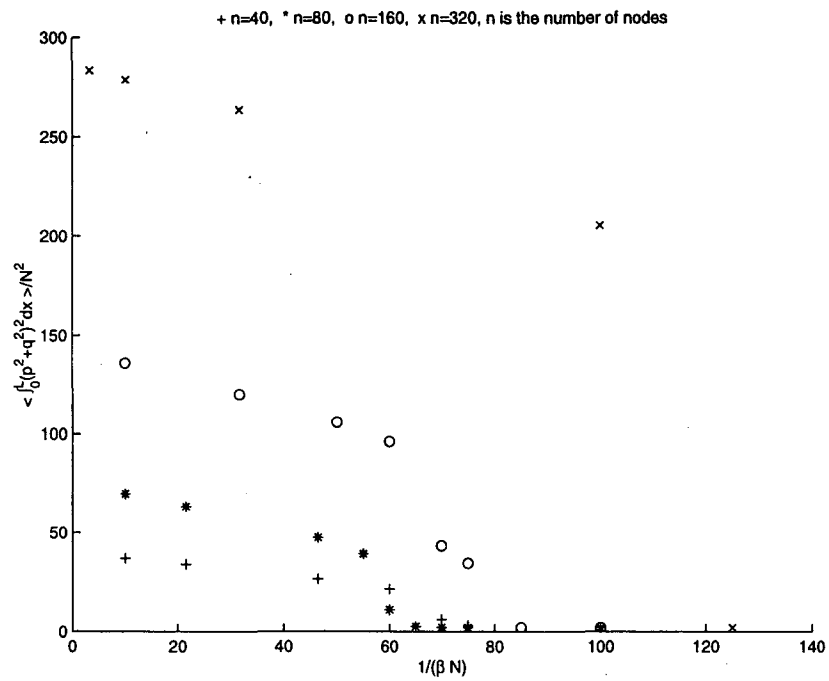

Figure 4.31: Values of K for increasing number of discretization points and N. $N = 640$ (for 40 and 80 nodes), $N = 1000$ (for 160 nodes), and $N = 2000$ (for 320 nodes)

500 imaginary components) becomes prohibitively expensive.

Chapter 5

The Self-Induction Approximation and the Non-linear Schrödinger Equation

In this chapter we describe the self-induction approximation for a single vortex. First we would like to motivate our interest in this equation and in statistical mechanics associated with this equation from the point of view of fluid and superfluid turbulence.

5.1 Introduction. Turbulence and Statistical Mechanics.

An understanding of turbulence is one of the important unsolved problems in science; turbulence in fluid and superfluid flows has been studied by scientists for many years. Smooth fluid flows are well understood and there are accurate models and computational methods for their analysis. However, three dimensional high Reynolds number fluid turbu-

lence is not well understood; one of the reasons for this is that accurate resolution of the turbulent three dimensional flow on a computer requires on the order of $10^{20} - 10^{50}$ grid points in space and time. This comes from the need to resolve the motion on length scales that span many orders of magnitude. It is evident that such calculations are impossible even on the fastest computers; therefore there is a need for a deeper insight into the physics of turbulence and into the computational algorithms.

There is experimental evidence that turbulent motion is not only very complex, but also random. In other words, if we make the same experiment with a large number of apparently identical systems, we would obtain different results from the same measuring process; this suggests that turbulence needs a statistical description. There is also evidence of universal behavior in turbulent motion; the inertial scale of turbulence, which is the scale between the range at which energy is injected into the system and the range at which it is dissipated, exhibits a universal energy spectrum, called the Kolmogorov spectrum, which is independent on the type of fluid and the geometry of the flow [14], [45], [38], [40], [44].

This motivates an approach to turbulence taken by many researchers in which one uses a stochastic model for the motion on the small scales, and one couples it with explicit solution of the Navier-Stokes equations on large scales. A small-scale model, or a subgrid model, is supposed to account for the effects on small scales, like energy transfer and dissipation [14], [40]. There is a more recent approach for treating simultaneously all scales of turbulence by a suitable stochastic model and computing averages of the fluid flow, subject to given initial constraints [18].

There are many approaches that can be taken to study turbulence by probabilistic

means. One of the most natural approaches is to apply ideas from statistical physics and equilibrium thermodynamics [14], [8], [9], [10], [11]. The idea is plausible, since the small scales of the turbulent flow have time scales much smaller than the time of the overall decay of the flow, so the small scales can reach equilibrium very fast compared to the time on which the flow is observed. The equilibrium assumption provides a great simplification, since it requires relatively few defining parameters, like energy, temperature, and a set of constraints; however, it still allows us to observe a wide variety of phenomena including phase transitions and negative temperatures [1], [7], [14], [12], [13], [16], [17], [36], [43], [50]. It also admits various formulations of turbulent models both in real space and spectral variables [14], [27], [52].

Turbulence plays an important role in quantum systems like superfluid helium [21]. In the superfluid flow the mechanical and thermal effects are coupled; thermal effects can destroy the superfluid flow, and this process has been related to turbulence [21], [24]. The equations of motions of the superfluid are not fully understood and how to model the superfluid flow remains an open question [29], [6], [56], [2], [53], [54].

The study of superfluidity is also important because of its relation to the superconductivity [22], [35]; therefore a study of superfluidity might provide an insight into the study of superconducting currents, and help in the design of the superconducting devices.

5.2 The Self-Induction Approximation

In this chapter we describe the self-induction approximation for a single vortex. We then use the Hasimoto transformation to obtain a non-linear Schrödinger equation

from the self-induction approximation. We use a Hamiltonian formulation of the non-linear Schrödinger equation to construct a Gibbs canonical ensemble.

We start by considering inviscid isentropic incompressible fluid in three dimensions. We would like to study its time evolution by studying the time evolution of the vorticity ω. Denote the velocity field by $\mathbf{v}$.

$$\omega = curl\mathbf{v}. \tag{5.1}$$

We show following [19] how the velocity $\mathbf{v}$ can be expressed in terms of the vorticity ω . An incompressible fluid satisfies the equation div $\mathbf{v}$=0. Then there is a vector field $\mathbf{A}$ such that $\mathbf{div}(\ \mathbf{A}\ )= \mathbf{0}$ and $\mathbf{v}$= curl ($\mathbf{A}$). Therefore $\triangle\ \mathbf{A}$ = -ω. Green's function for the Poisson equation in three dimensions is

$$G(\mathbf{x}, \mathbf{x}\prime) = -\frac{1}{4\pi\|\mathbf{x} - \mathbf{x}\prime\|}. \tag{5.2}$$

The vector $\mathbf{A}$ can be expressed in terms of ω by

$$\mathbf{A}(\mathbf{x}) = \int_{\mathbf{R}^3} G(\mathbf{x}, \mathbf{x}\prime)\omega(\mathbf{x}\prime), \mathbf{dx}\prime \tag{5.3}$$

where the integral is over $\mathbf{R}^3$. Taking the curl of $\mathbf{A}$, we get for $\mathbf{v}(\mathbf{x})$

$$\mathbf{v}(\mathbf{x}) = \frac{1}{4\pi}\int_{\mathbf{R}^3} \frac{(\mathbf{x} - \mathbf{x}\prime) \times \omega(\mathbf{x}\prime)}{\|\mathbf{x} - \mathbf{x}\prime\|^3}\mathbf{dx}\prime, \tag{5.4}$$

where the integral is taken over the whole three-dimensional space. We wish to rewrite this expression for the velocity in a different form. To do this we need to introduce the concept of a vortex tube and its strength.

Take a two-dimensional surface **S** that is nowhere tangent to ω. Draw vortex lines through each point of this surface, assuming that ω does not vanish anywhere on that surface. The resulting object, which is a product of the surface **S** and vortex lines, is called a vortex tube. Suppose the surface **S** is finite with a boundary that we will call **L**. The quantity

$$\int_{\mathbf{L}} \mathbf{v} d\mathbf{s}, \tag{5.5}$$

is the circulation of the tube. By Helmholtz' theorem [19] the circulation of the isentropic fluid around any two curves encircling a vortex tube is the same; this value is therefore common to the whole vortex tube. It is called strength of the vortex tube, and we denote it by $\tilde{\Gamma}$. It is also constant in time, as the vortex tube moves with the fluid. By Stokes' theorem

$$\tilde{\Gamma} = \int_{\mathbf{L}} \mathbf{v} d\mathbf{s} = \int_{\mathbf{S}} \omega d\mathbf{B}, \tag{5.6}$$

where d**B** denotes the differential directed area $d\mathbf{B} = \mathbf{n} d\delta$. Here **n** is a normal to the surface **S** and $d\delta$ is an infinitesimal area of the crosssection of the vortex tube.

Assume that vorticity is concentrated in a small neighborhood of a curve in three dimensions; call this curve with this neighborhood a vortex filament, and call this curve itself a centerline of the vortex filament. Assume further that along each crossection normal to the centerline, the vorticity associated with this vortex filament is the same at every point of the crossection and is parallel to the centerline at the point of the intersection of the centerline and the vortex tube.

For any surface **S** that is transverse to this centerline $\int_{\mathbf{S}} \omega \mathbf{dB} = \Gamma$. We call this Γ

the strength of the vortex filament. Then the formula for $\mathbf{v}(\mathbf{x})$ becomes

$$\mathbf{v}(\mathbf{x}) = \frac{\Gamma}{4\pi}\int_{\mathbf{C}} \frac{(\mathbf{x}-\mathbf{x}\prime)\times\mathbf{t}(\mathbf{x}\prime)}{\|\mathbf{x}-\mathbf{x}\prime\|^3}\mathbf{dx}\prime, \tag{5.7}$$

where the integral is taken over the line $\mathbf{C}$, and $\mathbf{t}(\mathbf{x}\prime)$ is a unit tangent vector to the curve $\mathbf{C}$ at the point $\mathbf{x}\prime$.

Now we wish to study the evolution of the vortex filament by the asymptotic expansion introduced by Arms and used by Hama [25]. We follow the presentation in [3] and [6].

Denote by $\mathbf{x}$(s) the centerline of the vortex filament, where s is an arclength along the centerline. By Taylor's theorem $\mathbf{x}$(s)= $\mathbf{x}(0) + \frac{\partial\mathbf{x}}{\partial s}(0)s + \frac{1}{2}\frac{\partial^2\mathbf{x}}{\partial s}(0)s^2 + O(s^3)$. Without loss of generality choose $\mathbf{x}(0)$=0, and denote the tangent unit vector $\frac{\partial\mathbf{x}}{\partial s}(0)$ by $\mathbf{t}$ and $\frac{\partial^2\mathbf{x}}{\partial s^2}(0)$ by $\kappa\mathbf{n}$, where $\mathbf{n}$ is the normal unit vector and κ is the curvature. Similarly, expand $\mathbf{t}$(s) as $\mathbf{t}$(s)= $\mathbf{t} + \kappa\mathbf{n}$s + O($s^3$). The vector product $\mathbf{t} \times \mathbf{n}$ is called the binormal vector; denote it by $\mathbf{b}$. Consider a local coordinate system at the point 0 spanned by the triple $\mathbf{t}$, $\mathbf{n}$, s; pick a point $\mathbf{r}$= $(0, \sigma\cos(\psi), \sigma\sin(\psi))$ near the vortex filament and calculate the integral (5.7) at this point. Neglecting terms of order three or higher in s we can write

$$(\mathbf{x}(s)-\mathbf{r})\times\mathbf{t}(s) = \mathbf{n}\sigma\sin(\psi) - \mathbf{b}\sigma\cos(\psi) - \mathbf{t}\sigma\kappa s\sin(\psi) - \frac{1}{2}\mathbf{b}\kappa s^2. \tag{5.8}$$

Substituting the expression above into (5.7), integrating from -L to L, and taking the distance σ from the point $\mathbf{r}$ to the filament sufficiently small, we get

$$\mathbf{v}(r) = \frac{\Gamma}{2\pi\sigma}(\mathbf{b}\cos(\psi) - \mathbf{n}\sin(\psi)) + \frac{\Gamma\kappa}{4\pi}\mathbf{b}\log(\frac{L}{\sigma}) + O(1). \tag{5.9}$$

The contribution to the velocity that comes from the vortex outside the line of integration -L $\leq s \leq$ L is bounded in magnitude and we can neglect it. The first term in (5.9) represents the rotation of the fluid around the vortex filament. A straight filament will produce a velocity field given by this first term, but the filament itself will remain stationary in its own velocity field. Therefore we assume that the motion of the vortex filament itself is given by the second term in (5.9).

Finally, we are able to write down an asymptotic equation for the motion of the vortex filament. Taking a point $\mathbf{x}$ on the filament we get from (5.9):

$$\mathbf{v}(\mathbf{x}) = \frac{\Gamma\kappa}{4\pi}\mathbf{b}\log(\frac{L}{\sigma}), \tag{5.10}$$

where $\mathbf{b}$ is the unit binormal vector at the point $\mathbf{x}$ and σ is usually taken as a finite radius of the real vortex filament. We can change units of time in (5.10) to absorb the constant in front of the equation

$$\mathbf{v}(\mathbf{x}) = \kappa\mathbf{b}. \tag{5.11}$$

We would like to show now that a vortex filament moving with the fluid according to (5.11) does not stretch. Pick a parametrization of the filament η by parametrizing the fluid particles along the filament; the length along the vortex filament s is thus a function of η. If the filament stretches as it moves $\frac{\partial s(\eta,t)}{\partial\eta}$ should depend on time. We now prove that $\frac{\partial s(\eta,t)}{\partial\eta}$ does not depend on time. Differentiate (5.11) with respect to the arclength s :

$$\frac{\partial}{\partial s}(\frac{\partial\mathbf{x}}{\partial t}) = \frac{\partial(\kappa(\partial s\times\mathbf{n}))}{\partial t} = \frac{\partial\kappa}{\partial s}(\mathbf{t}\times\mathbf{n}) + \kappa(\frac{\partial\mathbf{t}}{s}\times\mathbf{n} + \mathbf{t}\times\frac{\partial}{\partial s}(\frac{1}{\kappa}\frac{\partial\mathbf{t}}{\partial s}) =$$

$$\frac{\partial\kappa}{\partial s}(\mathbf{t}\times\mathbf{n}) + \kappa(\mathbf{t}\times\frac{1}{\kappa}\frac{\partial^2\mathbf{t}}{\partial s^2} - \frac{1}{\kappa^2}\frac{\partial\kappa}{\partial s}\mathbf{t}\times\frac{\partial\mathbf{t}}{\partial s}) = \mathbf{t}\times\frac{\partial^2\mathbf{t}}{\partial s^2}.$$

Here we use the fact that $\frac{\partial \mathbf{t}}{\partial s} = \kappa \mathbf{n}$. Changing the order of differentiation in the expression above, we find:

$$\frac{\partial \mathbf{t}}{\partial t} = \mathbf{t} \times \frac{\partial^2 \mathbf{t}}{\partial s^2}. \tag{5.12}$$

Analogously, we differentiate (5.11) with respect to η and get:

$$\frac{\partial}{\partial \eta}(\frac{\partial \mathbf{x}}{\partial t}) = \mathbf{t} \times \frac{\partial^2 \mathbf{t}}{\partial s^2}\frac{\partial s}{\partial \eta}. \tag{5.13}$$

Finally, we differentiate $\frac{\partial \mathbf{x}}{\partial \eta}$ with respect to time:

$$\frac{\partial}{\partial t}(\frac{\partial \mathbf{x}}{\partial \eta}) = \frac{\partial}{\partial t}(\frac{\partial \mathbf{x}}{\partial s}\frac{\partial s}{\partial \eta}) = \frac{\partial \mathbf{t}}{\partial t}\frac{\partial s}{\partial \eta} + \frac{\partial \mathbf{x}}{\partial s}\frac{\partial}{\partial t}(\frac{\partial s}{\partial \eta}). \tag{5.14}$$

Changing the order of differentiation in the formula above and using (5.13) we get:

$$\frac{\partial}{\partial t}(\frac{\partial \mathbf{x}}{\partial \eta}) = \frac{\partial}{\partial \eta}(\frac{\partial \mathbf{x}}{\partial t}) = \mathbf{t} \times \frac{\partial^2 \mathbf{t}}{\partial s^2}\frac{\partial s}{\partial \eta}. \tag{5.15}$$

From formulas (5.12 - 5.15) above, we conclude that $\frac{\partial}{\partial t}(\frac{\partial s}{\partial \eta}) = 0$ i.e. the filament does not stretch. This is one of the limitations of this model of the motion of the vortex, since real fluid vortices exhibit stretching.

5.3 The Hasimoto Transformation

In this section we describe a transformation, due to Hasimoto, of a self-induction approximation into a nonlinear Schrödinger equation.

The Frenet-Seret equations of differential geometry are given by:

$$\frac{\partial \mathbf{x}}{\partial s} = \mathbf{t}, \qquad \frac{\partial \mathbf{t}}{\partial s} = \kappa \mathbf{n}, \qquad \frac{\partial \mathbf{n}}{\partial s} = \tau \mathbf{b} - \kappa \mathbf{t}, \qquad \frac{\partial \mathbf{b}}{\partial s} = -\tau \mathbf{n}, \tag{5.16}$$

where $\mathbf{x}$ is the vortex centerline, $\mathbf{t}$ is the unit tangent, $\mathbf{n}$ is the unit normal, $\mathbf{b}$ is the unit binormal, κ is the curvature, τ is the torsion, and s is the arclength. Using the last two equations in (5.16) we obtain:

$$\frac{\partial}{\partial s}(\mathbf{n} + i\mathbf{b}) = -i\tau(\mathbf{n} + i\mathbf{b}) - \kappa\mathbf{t}. \tag{5.17}$$

This suggests the following coordinate transformation:

$$\mathbf{N} = (\mathbf{n} + i\mathbf{b})exp(i\int_0^s \tau(s)ds) \tag{5.18}$$

$$\psi = \kappa exp(i\int_0^s \tau(s)ds). \tag{5.19}$$

Then from (5.18) and (5.19) we obtain:

$$\frac{\partial \mathbf{N}}{\partial s} = -\psi\mathbf{t}, \tag{5.20}$$

and

$$\frac{\partial \mathbf{t}}{\partial s} = \mathbf{Re}(\psi\bar{\mathbf{N}}) = \frac{1}{2}(\bar{\psi}\mathbf{N} + \psi\bar{\mathbf{N}}). \tag{5.21}$$

Next we would like to derive an equation describing the time evolution of $\mathbf{N}$. Expand $\frac{\partial \mathbf{N}}{\partial t}$ in $\mathbf{N}$, $\bar{\mathbf{N}}$, $\mathbf{t}$, where $\bar{\mathbf{N}}$ denotes the complex conjugate of $\mathbf{N}$:

$$\frac{\partial \mathbf{N}}{\partial t} = \alpha\mathbf{N} + \beta\bar{\mathbf{N}} + \gamma\mathbf{t}. \tag{5.22}$$

We then have the following scalar products between $\mathbf{t}$, $\mathbf{N}$, and $\bar{\mathbf{N}}$:

$$\mathbf{t}\mathbf{N} = \mathbf{t}\bar{\mathbf{N}} = 0, \qquad \mathbf{N}\mathbf{N} = \bar{\mathbf{N}}\bar{\mathbf{N}} = 0, \qquad \mathbf{N}\bar{\mathbf{N}} = 2.$$

We determine the coefficients α, β, and γ as follows:

$$\begin{aligned} \alpha + \bar{\alpha} &= \frac{1}{2}(\dot{\mathrm{N}}\bar{\mathrm{N}} + \dot{\bar{\mathrm{N}}}\mathrm{N}) = \frac{\partial}{\partial t}(\mathrm{N}\bar{\mathrm{N}}) = 0 \\ \beta &= \frac{1}{2}\dot{\mathrm{N}}\mathrm{N} = \frac{1}{4}\frac{\partial}{\partial t}(\mathrm{N}\mathrm{N}) = 0 \\ \gamma &= -\mathrm{N}\frac{\partial \mathbf{t}}{\partial t}. \end{aligned} \tag{5.23}$$

Thus $\alpha = \mathrm{iR}$, where R is some unknown real function. To determine γ, compute the derivative of $\mathbf{t}$ with respect to time:

$$\frac{\partial \mathbf{t}}{\partial t} = \frac{\partial}{\partial s}(\kappa \mathbf{b}) = \frac{\partial \kappa}{\partial s}\mathbf{b} - \kappa\tau\mathbf{n} = \mathbf{Re}(i\frac{\partial \psi}{\partial s}\bar{\mathrm{N}}) = \frac{i}{2}(\frac{\partial \psi}{\partial s}\bar{\mathrm{N}} - \frac{\partial \bar{\psi}}{\partial s}\mathrm{N}). \tag{5.24}$$

Using the orthogonality relations and (5.24) we find the expression for γ:

$$\gamma = -i\frac{\partial \psi}{\partial s}. \tag{5.25}$$

Combining (5.22), (5.24), and (5.25) we obtain an expression for the time derivative of N:

$$\frac{\partial \mathrm{N}}{\partial t} = i(R\mathrm{N} - \frac{\partial \psi}{\partial s}\mathbf{t}). \tag{5.26}$$

We wish to write down an evolution equation for ψ. To do this we differentiate equation (5.20) with respect to time, equation (5.26) with respect to arclength, and then use formulas (5.20), (5.21), and (5.24); the result is:

$$\begin{aligned} \frac{\partial}{\partial t}(\frac{\partial \mathrm{N}}{\partial s}) &= -\frac{\partial \psi}{\partial t}\mathbf{t} - \psi\frac{\partial \mathbf{t}}{\partial t} = -\frac{\partial \psi}{\partial t}\mathbf{t} - \psi\frac{i}{2}(\frac{\partial \psi}{\partial s}\bar{\mathrm{N}} - \frac{\partial \bar{\psi}}{\partial s}\mathrm{N}) \\ \frac{\partial}{\partial s}(\frac{\partial \mathrm{N}}{\partial t}) &= i(\frac{\partial R}{\partial s}\mathrm{N} - R\psi\mathbf{t} - \frac{\partial^2 \psi}{\partial s^2}\mathbf{t} - \frac{\partial \psi}{\partial s}\frac{1}{2}(\bar{\psi}\mathrm{N} + \psi\bar{\mathrm{N}})). \end{aligned} \tag{5.27}$$

Equating the coefficients of $\mathbf{t}$ and N in (5.27), we have:

$$\frac{\partial \psi}{\partial t} = i(\frac{\partial^2 \psi}{\partial s^2} + R\psi) \tag{5.28}$$

$$\frac{1}{2}\psi\frac{\partial\bar{\psi}}{\partial s} = \frac{\partial R}{\partial s} - \frac{1}{2}\frac{\partial\psi}{\partial s}\bar{\psi}. \tag{5.29}$$

From (5.29) we can solve for R:

$$R(s,t) = \frac{1}{2}(\psi(s,t)\bar{\psi}(s,t) + C(t)), \tag{5.30}$$

where C is some function of time only. Substituting this expression for R into (5.28) we get an equation for ψ:

$$\frac{1}{i}\frac{\partial\psi}{\partial t} = \frac{\partial^2\psi}{\partial s^2} + \frac{1}{2}(|\psi|^2 + C)\psi. \tag{5.31}$$

We can eliminate the function C from the equation above by introducing a change of variables:

$$\tilde{\psi} = \psi\exp(-\frac{i}{2}\int_0^t C(\tau)d\tau), \tag{5.32}$$

and rewrite equation (5.31) in the form:

$$\frac{1}{i}\frac{\partial\tilde{\psi}}{\partial t} = \frac{\partial^2\tilde{\psi}}{\partial s^2} + \frac{1}{2}|\tilde{\psi}|^2\tilde{\psi}. \tag{5.33}$$

It should be pointed out that the function C(t) which appears in (5.31) is not arbitrary. It can be recovered from the fact that we have chosen our variable ψ(s,t) in such a way that ψ(0,t) is a real function for all time. We now show how C(t) can be reconstructed from this constraint: Suppose we solve equation (5.33) with some initial condition ψ(s,0)= $\tilde{\psi}$(s,0) and some appropriate boundary conditions; then we find $\tilde{\psi}$(s,t) = r(s,t)exp(iθ(s,t)), where r(s,t) is the absolute value of $\tilde{\psi}$(s,t). Therefore,

$$r(0,t)\exp(i\theta(0,t)) = \psi(0,t)\exp(-\frac{i}{2}\int_0^t C(\eta)d\eta). \tag{5.34}$$

Since $\psi(0,t)$ is real r(0,t)=$\psi(0,t)$ and $\theta(0,t)$=-$\frac{1}{2}\int_0^t C(\eta)d\eta$. From this we find C(t) explicitly:

$$C(t) = -2\frac{\partial\theta(0,t)}{\partial t}. \tag{5.35}$$

Now we can in principle start from the self-induction equation, go to the nonlinear Schrödinger equation, solve it and then go back to the self-induction approximation, and write down the solution in the original variables. A more detailed description is presented in [6].

Before concluding this chapter we would like to discuss briefly the invariants of the self-induction and nonlinear Schrödinger equations. One of the properties of these equations is the existence of an infinite number of constants of motion. For the nonlinear Schrödinger equation we can write the first two (see [51] for more):

$$\begin{aligned} \frac{\partial}{\partial t}\int |\psi(s)|^2 ds &= 0, \\ \frac{\partial}{\partial t}\int (\frac{\partial\bar{\psi}}{\partial s}\psi - \frac{\partial\psi}{\partial s}\bar{\psi})ds &= 0. \end{aligned} \tag{5.36}$$

For the self-induction equation we can write down corresponding constants of motion:

$$\begin{aligned} \frac{\partial}{\partial t}\int \kappa^2(s)ds &= 0, \\ \frac{\partial}{\partial t}\int \kappa^2\tau ds &= 0. \end{aligned} \tag{5.37}$$

In addition, as was shown above, the arclength is a constant of motion in the self-induction approximation. The invariants of the self-induction equation can also be checked by direct substitution. The first of the invariants in (5.37) can be interpreted as the 'total curvature' of the vortex filament; we see that as the vortex moves with the fluid its 'total curvature' remains constant; later we will make use of this invariant.

5.4 Changes in the shape of a vortex filament with respect to constraint N and temperature

In this section we present the plots of the typical vortex filaments that we obtain from the cubic Schrödinger equation for different values of the constraint N and temperature. We remarked at the end of Chapter 4 that in the limit as constraint N goes to infinity the temperature at which the transition occurs also goes to infinity. This fact is in agreement with the results of Chorin [12], [14], [15] that the single vortex filament has a phase transition at infinite temperature.

Recall that equations (5.20),(5.21) are a consequence of the Frenet-Seret equations of differential geometry (5.16). Integrating equations (5.20),(5.21) starting at some arbitrary point in space produces the vortex filament that corresponds to the complex function ψ. There are two difficulties in restoring the vortex from ψ; one is that ψ might be a rapidly oscillating non-smooth function, in which case we have to smooth it a little bit. The second is that by the definition of ψ in (5.19) it has to be purely real at the point $s = 0$, so the problem is to find a filament corresponding to an arbitrary function ψ that does not have a purely real point. We do not resolve this problem here, and just use in our presentation functions ψ that are real at $s = 0$.

The soliton-like field, which is a typical field configuration for low temperatures and large N (Figure 4.1) corresponds to an almost straight vortex filament with a sharp kink (see Figure 5.1)

This shape roughly corresponds to the left part of the upper kurtosis function in Figure (4.5). Keeping the temperature low and decreasing the value of the constraint N

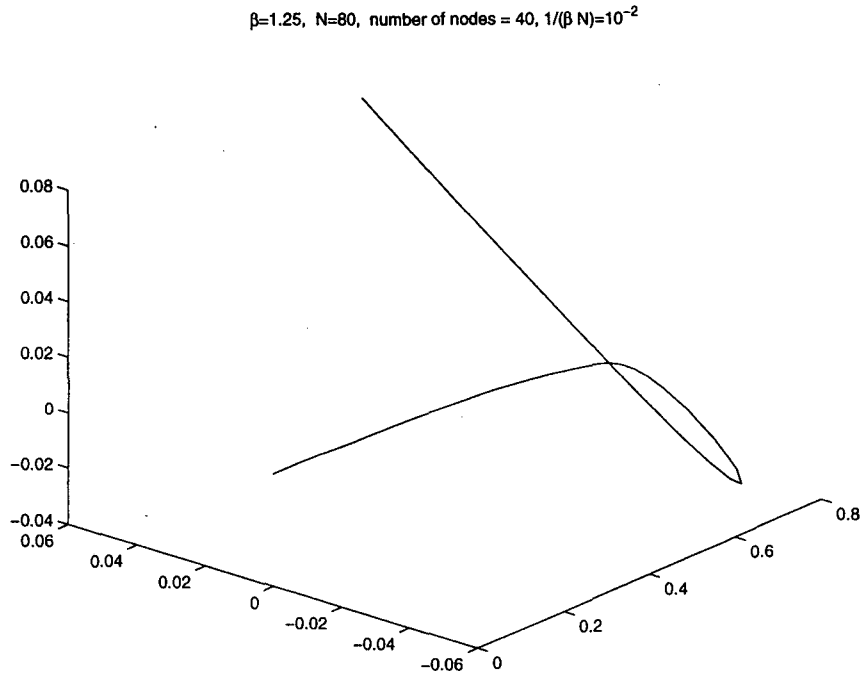

Figure 5.1: Typical vortex filament for low temperature and large N, $\frac{1}{\beta N} = 10^{-2}$

gives the left part of the lower kurtosis function in Figure (4.5); the typical field configuration is close to a constant, and the corresponding filament shape is given in Figure (5.2). The vortex is smooth and almost circular, which is what one would expect for a constant field, i.e. for constant curvature.

Increasing the temperature destroys the order in the shape of the vortex filament, and the typical vortex becomes more random, as shown in Figure (5.3); this filament corresponds to the right-hand side of the kurtosis curves in Figure (4.5).

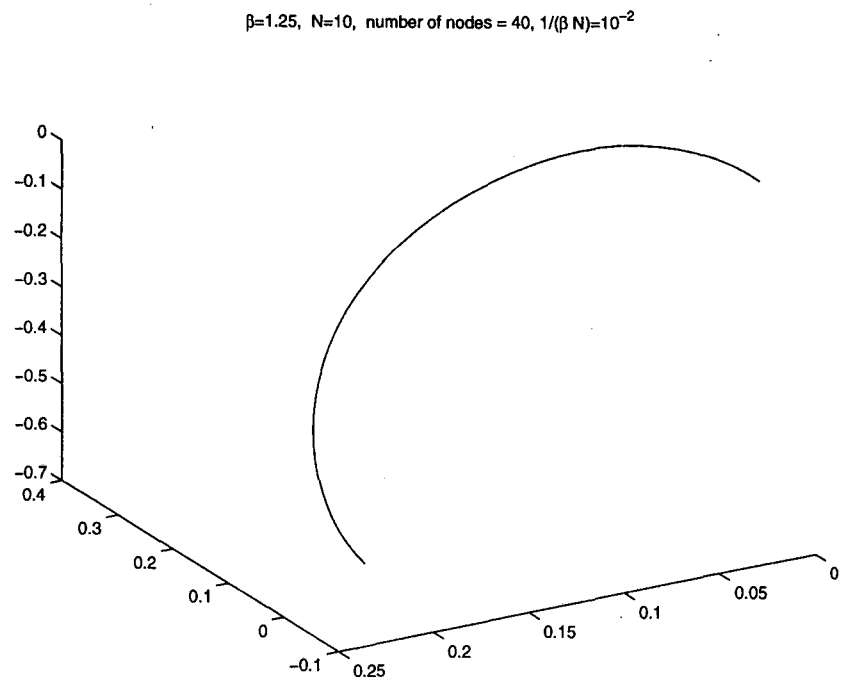

Figure 5.2: Typical vortex filament for low temperature and small N, $\frac{1}{\beta N} = 10^{-2}$

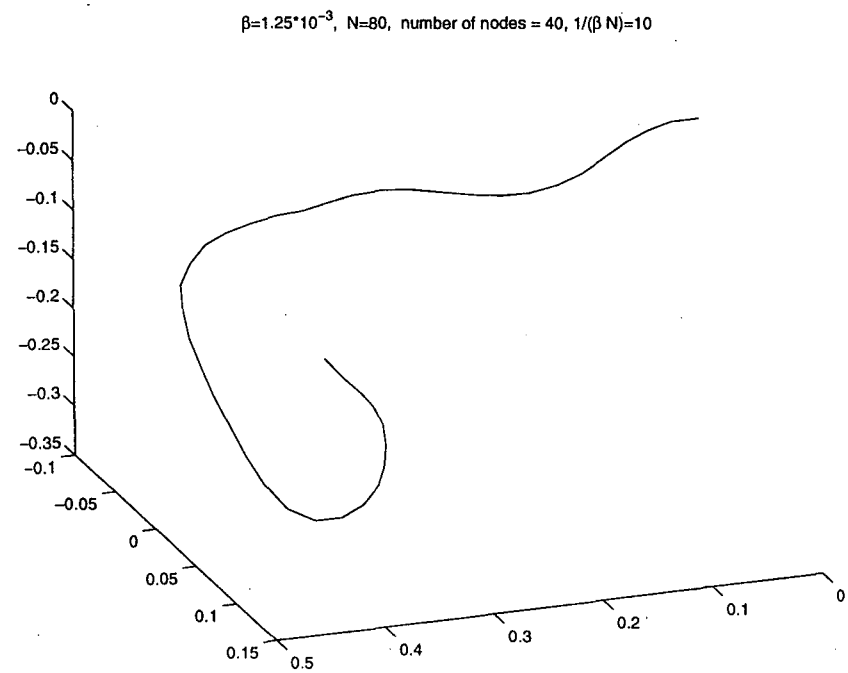

Figure 5.3: Typical vortex filament for high temperature, $\frac{1}{\beta N} = 10$.

Chapter 6

Conclusions

We have studied numerically bifurcation and phase transition phenomena in the Gibbs canonical ensemble associated with the cubic Schrödinger equation.

We have shown that the changes in typical function profiles with respect to temperature and constraint observed in [41] are associated with the splitting of a phase space into different components. We discovered that these changes can be observed in a discretization with as few as 2 points.

For low fixed temperatures, as the constraint (3.6) increases, the functions on which the Gibbs canonical ensemble (3.5),(3.6) is concentrated change from almost constant functions (Figure 4.3) to a soliton shaped functions (Figure 4.1). This explains the increase in average kurtosis presented in Figure (4.5). There is a corresponding change in the phase space structure of the minimum energy surface for the Hamiltonian (3.3). We observe that as the constraint increases, the torus-like structure which corresponds to the small value of the constraint splits into two tori structure, and as the constraint increases further the two

tori split further apart until they become perpendicular to each other.

The second type of change that we have studied is with respect to temperature (with the constraint fixed (3.6)). As the temperature increases the typical soliton-like shape is destroyed and becomes just a random fluctuation for high temperatures (Figure 4.2). This explains the decrease in average kurtosis presented in (4.5). Corresponding to the change in the kurtosis, the phase space structure of the Metropolis sampling trajectories changes from a torus-like shape to a ball-like shape (Figures 4.10,4.11). The temperature region in which the change in the structure of the Metropolis sampling trajectories occurs exactly corresponds to the temperature region for the change in kurtosis in Figure (4.5).

We point out that the cubic Schrödinger equation is equivalent to the self-induction approximation for vortices [26]. In terms of vortex representation the soliton-like typical structure of functions at low temperatures corresponds to a straight vortex filament with a sharp kink; for high temperatures the straightness of the vortex is destroyed and the shape of the vortex becomes random (Figures 5.1, 5.3). We remark that in the limit the temperature at which the transition occurs increases to infinity, which is in agreement with the results of Chorin [12], [14], [15] that the single vortex filament has a phase transition at infinite temperature.

We have investigated numerically the limit of the kurtosis (4.4) for a fixed number of discretization points as the constraint (3.6) increases; we demonstrated that eventually the kurtosis converges to a smooth function whose maximum value is determined by the number of discretization points.

We also investigated the limit of kurtosis (4.4) for a fixed value of the constraint

as the number of discretization points increases; we found that the kurtosis converges to a smooth function in this limit as well.

However, if we increase both the constraint (3.6) and the number of discretization points, then we see a strong numerical indication that for some temperature the first derivative of the kurtosis (4.4) becomes infinite. We do not know what happens in the infinite limit; however, for large enough values of the constraint and for a large enough number of discretization points there may be a discontinuity in the first derivative of the kurtosis (4.4), which could indicate a behavior similar to a phase transition in classical statistical mechanics.

We also have shown the equivalence of the Gibbs canonical ensemble associated with the cubic Schrödinger equation (3.5),(3.6) and the microcanonical ensemble (Figure (3.2)).

We have studied the ergodicity of the system (3.2) (3.5),(3.6), and presented results that show the equivalence of time and ensemble averages (Figure 3.2). We remarked that the numerical method used for integrating the cubic Schrödinger equation in time has two constants of motion: the Hamiltonian (3.3) and the constraint (3.6). On the other hand the cubic Schrödinger equation has an infinite number of conserved quantities [51], so the relation of this numerical result to the discretized equations of motion for the continuum cubic Schrödinger equation is not straightforward. However, it is still an interesting fact that in the discrete version of the cubic Schrödinger equation there is an equivalence of the time and ensemble averages.

Bibliography

[1] J.Akao *Phase Transitions and Connectivity in Three-Dimensional Vortex Equilibria*, Ph.D. Thesis, Berkeley, 1994.

[2] C.Barenghi, R.Donnelly, W.Vinen *Friction on quantized vortices in helium II*, Journal of Low Temperature Physics, 52, 189-247, 1983.

[3] G.K.Batchelor *An Introduction to Fluid Dynamics*, Cambridge University Press, London, 1967.

[4] K.Binder, D.W.Heermann *Monte Carlo Simulation in Statistical Physics*, Springer-Verlag, New York Berlin Heidelberg, 1992.

[5] T.Buttke *A Numerical Study of Superfluid Turbulence in the Self-Induction Approximation*, Journal of Computational Physics 76, 301-326, 1988.

[6] T.Buttke *A Numerical Study of Superfluid Turbulence in the Self-Induction Approximation*, Ph.D. Thesis, Berkeley, 1986.

[7] E.Caglioti, P.Lions, C.Marchioro, M.Pulvirenti *A special class of stationary flows for 2-dimensional Euler equations - a statistical mechanics description*, Communications in Mathematical Physics, 143(3), pp.501-525, 1992.

[8] A.J.Chorin *Turbulence as a Near-Equilibrium Process*, Lectures in Applied Mathematics, Vol.31, 1996.

[9] A.J.Chorin *The Evolution of a Turbulent Vortex*, Comm. Math. Phys., 83 (1982), pp.517-535.

[10] A.J.Chorin *New perspectives in turbulence*, Preprint, Berkeley, 1997.

[11] A.J.Chorin, G.I.Barenblatt *A near-equilibrium theory of turbulence with applications*, Preprint, Berkeley, 1997.

[12] A.J.Chorin *Equilibrium statistics of a vortex filament with applications*, Communications in Mathematical Physics, 141(3), pp.619-631, 1991.

[13] A.J.Chorin *A vortex model with superfluid and turbulent percolation*, Journal of Statistical Physics, 69(1-2), pp.67-78, 1992.

[14] A.J.Chorin *Vorticity and Turbulence*, Springer-Verlag, New York, 1994.

[15] A.J.Chorin, J.Akao *Vortex equilibria in turbulence theory and quantum analogues*, Physica D 51 (1991), pp. 403-414.

[16] A.J.Chorin, O.H.Hald *Analysis of Kosterlitz-Thouless transition models*, Physica D, vol.99, (no.4), Elsevier, 1 Jan. 1997. p.442-70.

[17] A.J.Chorin, O.H.Hald *Vortex renormalization in three space dimensions*, Phys. Rev. B 51 (1995), pp. 11969-11972.

[18] A.J.Chorin, A.Kast, R.Kupferman *Optimal Prediction of Underresolved Dynamics*, Preprint, Berkeley, 1998.

[19] A.J.Chorin J.E.Marsden *A Mathematical Introduction to Fluid Mechanics*, Springer-Verlag, Third Edition 1993.

[20] R.J.Donnely *Quantized Vortices in Helium II*, Cambridge, 1991.

[21] R.J.Donnely, C.E.Swanson *Quantum turbulence*, Journal of Fluid Mechanics, 173, pp.387-429, 1986.

[22] R.J.Donnely *The discovery of superfluidity*, Physics Today, vol.48, (7), July 1995.

[23] S.Dyachenko, A.C.Newell, A.Pushkarev, V.E.Zakharov *Optical turbulence: weak turbulence, condensates and collapsing filaments in the nonlinear Schrödinger equation*, Physica D 57 (1992) pp.96-160

[24] R.P.Feynman *Application of quantum mechanics to liquid helium*, Progress in Low Temperature Physics, 1955.

[25] F.R.Hama *Progressive Deformation of a Curved Vortex Filament by its Own Induction*, Phys. Fluids, 5 (1962), pp.1156-1162

[26] H.Hasimoto *A Soliton On a Vortex Filament*, J.Fluid Mech., 51 (1972), pp.477-485

[27] E.Hopf *Statistical Hydrodynamics and Functional Calculus*, Journal of Rational Mechanics and Analysis, 1, pp.87-141, 1952.

[28] K.Huang *Statistical Mechanics*, John Wiley & Sons, New York, 1987.

[29] I.M.Khalatnikov *Introduction to the theory of superfluidity*, Addison-Wesley, Redwood City, 1989.

[30] R.Klein, O.Knio *Asymptotic vorticity structure and numerical simulation of slender vortex filaments* Journal of Fluid Mechanics, vol.284, pp.275-321, 1995.

[31] R.Klein, A.Majda *Self-stretching of a perturbed vortex filament 1. The asymptotic equation for deviations from a straight line* Physica D 49, 1991, pp. 323-352

[32] R.Klein, A.Majda *Self-stretching of perturbed vortex filaments 2. Structure of solutions*, Physica D 53, 1991, pp. 267-294

[33] R.Klein, A.Majda *An asymptotic theory for the nonlinear instability of antiparallel pairs of vortex filaments*, Physics of Fluids A (Fluid Dynamics), vol.5, (no.2), Feb. 1993. p.369-79.

[34] R.Klein, A.Majda, K.Damodaran *Simplified equations for the interaction of nearly parallel vortex filaments*, Journal of Fluid Mechanics, vol.288, pp.201-248, 1995.

[35] H.Kleinert *Gauge Fields in Condensed Matter*, World Scientific Publishing, 1989.

[36] J.Kosterlitz, D.Thouless *Order, metastability and phase transitions in two-dimensional systems*, Journal of Physics C, 6, pp.1181-1203, 1973.

[37] H.Lamb *Hydrodynamics*, Dover Publications, New York, 1932.

[38] L.D.Landau, E.M.Lifshitz *Hydrodynamics*, Pergamon Press, 1980.

[39] L.D.Landau, E.M.Lifshitz *Statistical Physics*, Pergamon Press, 1980.

[40] M.Lesieur *Turbulence in Fluids: Stochastic and Numerical Modeling*, Kluwer Academic Publishers, 2nd edition, 1990.

[41] J.L.Lebowitz, H.A.Rose, E.R.Speer *Statistical Mechanics of the Nonlinear Schrödinger Equation*, Journal of Statistical Physics, Vol. 50, Nos 3/4, 1988

[42] J.L.Lebowitz, H.A.Rose, E.R.Speer *Statistical Mechanics of the Nonlinear Schrödinger Equation. II. Mean Field Approximation*, Journal of Statistical Physics, Vol. 54, Nos 1/2, 1989.

[43] T.Lundgren, Y.Pointin *Statistical Mechanics of two-dimensional vortices*, Journal of Statistical Physics, 17, pp.323-355, 1977.

[44] C.Marchioro, M.Pulvirenti *Mathematical Theory of Incompressible Nonviscous Fluids*, Springer-Verlag, New York, 1994.

[45] W.D.McComb *Physical Theories of Turbulence*, Cambridge, 1989.

[46] H.P.McKean *Statistical Mechanics of Nonlinear Wave Equations (4): Cubic Schrödinger*, Communications in Mathematical Physics, vol.168 (1995), p. 479-491

[47] H.P.McKean, K.L.Vaninsky *Statistical Mechanics of Nonlinear Wave Equations*, Preprint, CIMS, 1993.

[48] H.P.McKean, K.L.Vaninsky *Brownian motion with restoring drift: the petit and micro-canonical ensembles*, Communications in Mathematical Physics, vol.160, (no.3), 1994. p.615-30

[49] N.Metropolis, A.W.Rosenbluth, M.N.Rosenbluth, A.H.Teller, E.Teller J.Chem.Phys 21, 1087, 1953

[50] D.Montgomery, G.Joyce *Statistical mechanics of negative temperature states*, Physics of Fluids, 17(6), pp.1139-1145, 1974.

[51] A.C.Newell *Solitons in Mathematics and Physics*, SIAM, Philadelphia, 1985.

[52] S.Orszag *Analytical theories of turbulence*, Journal of Fluid Mechanics, 41, pp.363-386, 1970.

[53] K.W.Schwarz *Turbulence in superfluid helium: Steady homogeneous counterflow*, Physical Reviews B, 18, pp.245-262, 1978.

[54] K.W.Schwarz *Generation of Superfluid Turbulence Deduced from Simple Dynamical Rules*, Phys. Rev. Let., 49, pp.283-285, 1982.

[55] A.D.Sokal *Monte Carlo Methods in Statistical Mechanics: Foundations and New Algorithms*, Troisieme Cycle de la Physique, Semestre d'ete 1989

[56] D.R.Tilley, J.Tilley *Superfluidity and Superconductivity*, Boston, 1986.

[57] H.Zhou *Numerical Analysis of Slender Vortex Motion*, Ph.D. Thesis, Berkeley, 1996.

ERNEST ORLANDO LAWRENCE BERKELEY NATIONAL LABORATORY
ONE CYCLOTRON ROAD | BERKELEY, CALIFORNIA 94720

Prepared for the U.S. Department of Energy under Contract No. DE-AC03-76SF00098